

The Ensemble Photometric Variability of ~ 25000 Quasars in the Sloan Digital Sky Survey

Daniel E. Vanden Berk¹, Brian C. Wilhite², Richard G. Kron^{2,3}, Scott F. Anderson⁴, Robert J. Brunner⁵, Patrick B. Hall^{6,7}, Željko Ivezić⁶, Gordon T. Richards⁶, Donald P. Schneider⁸, Donald G. York^{2,9}, Jonathan V. Brinkmann¹⁰, Don Q. Lamb², Robert C. Nichol¹¹, David J. Schlegel⁶

ABSTRACT

Using a sample of over 25000 spectroscopically confirmed quasars from the Sloan Digital Sky Survey, we show how quasar variability in the rest frame optical/UV regime depends upon rest frame time lag, luminosity, rest wavelength, redshift, the presence of radio and X-ray emission, and the presence of broad absorption line systems. Imaging photometry is compared with three-band spectrophotometry obtained at later epochs spanning time lags up to about two years. The large sample size and wide range of parameter values allow the dependence of variability to be isolated as a function of many independent parameters. The time dependence of variability (the structure function) is well-fit by a single power law with an index $\gamma = 0.246 \pm 0.008$, on timescales from days to years. There is an anti-correlation of variability amplitude with rest wavelength – e.g. quasars are about twice as variable at 1000\AA as 6000\AA – and quasars are systematically bluer when brighter at all redshifts. There is a strong anti-correlation of variability with quasar luminosity – variability amplitude decreases by a factor of about four when luminosity increases by a factor of 100. There is also a significant positive correlation of variability amplitude with redshift, indicating evolution of the quasar population or the variability mechanism. We parameterize all of these relationships. Quasars with RASS X-ray detections are significantly more variable (at optical/UV wavelengths) than those without, and radio loud quasars are marginally more variable than their radio weak counterparts. We find no significant difference in the variability of quasars with and without broad absorption line troughs. Currently, no models of quasar variability address more than a few of these relationships. Models involving multiple discrete events or gravitational microlensing are unlikely by themselves to account for the data. So-called accretion disk instability models are promising, but more quantitative predictions are needed.

Subject headings: galaxies: active – quasars: general – techniques: photometric

¹Department of Physics and Astronomy, University of Pittsburgh, 3941 O'Hara Street, Pittsburgh, PA 15260.

²Department of Astronomy and Astrophysics, The University of Chicago, 5640 South Ellis Avenue, Chicago, IL 60637.

³Fermi National Accelerator Laboratory, P.O. Box 500, Batavia, IL 60510.

⁴Department of Astronomy, University of Washington, Box 351580, Seattle, WA 98195.

⁵Department of Astronomy/NCSA, University of Illinois, 1002 W. Green Street, Urbana, IL 61801.

⁶Princeton University Observatory, Peyton Hall, Prince-

ton, NJ 08544.

⁷Departamento de Astronomía y Astrofísica, Pontificia Universidad Católica de Chile, Casilla 306, Santiago 22, Chile.

⁸Department of Astronomy and Astrophysics, The Pennsylvania State University, 525 Davey Laboratory, University Park, PA 16802.

⁹Enrico Fermi Institute, The University of Chicago, 5640 South Ellis Avenue, Chicago, IL 60637.

¹⁰Apache Point Observatory, P.O. Box 59, Sunspot, NM 88349.

¹¹Department of Physics, Carnegie Mellon University,

1. Introduction

The luminosities of quasars and other active galactic nuclei (AGNs) have been observed to vary from X-ray to radio wavelengths, and on time scales from several hours to many years. The majority of quasars exhibit continuum variability on the order of 10% on timescales of months to years. A minority of AGNs, broadly classified as blazars, vary much more dramatically on much shorter timescales. The mechanisms behind quasar variability are not known, although in principle variability is a powerful means of constraining models for the energy source of AGNs. The most promising models (for non-blazar variability) include accretion disk instabilities (e.g. Rees 1984; Kawaguchi, Mineshige, Umemura, & Turner 1998), so-called Poissonian processes such as multiple supernovae (e.g. Terlevich, Tenorio-Tagle, Franco, & Melnick 1992) or star collisions (Courvoisier, Paltani, & Walter 1996; Torricelli-Ciamponi, Foellmi, Courvoisier, & Paltani 2000), and gravitational microlensing (e.g. Hawkins 1993). Only recently have the various models become quantitative enough for meaningful comparison with observations. A consensus on the observational trends with variability is emerging, but disagreements remain and even the most fundamental relationships need better characterization.

Several dozen studies of quasar optical broadband variability have appeared in the literature. A number of the more important studies are summarized in tabular form by Helfand et al. (2001) and Giveon et al. (1999). Most ensemble studies have focused on establishing correlations between variability (defined in various ways as a measure of the source brightness change) and a number of parameters, most importantly time lag, quasar luminosity, rest frame wavelength, and redshift. Characteristic timescales of variability range from months to years (e.g. Collier & Peterson 2001; Cristiani et al. 1996; di Clemente et al. 1996; Smith & Nair 1995; Hook, McMahon, Boyle, & Irwin 1994; Trèvese et al. 1994). The amplitude of variability rises quickly on those timescales, but may slow or even level off on longer timescales.

An anti-correlation between quasar variabil-

ity and luminosity was reported by Angione & Smith (1972), and confirmed in numerous subsequent studies (Uomoto, Wills, & Wills 1976; Pica & Smith 1983; Lloyd 1984; O'brien, Gondhalekar, & Wilson 1988; Hook, McMahon, Boyle, & Irwin 1994; Trèvese et al. 1994; Cid Fernandes, Aretxaga, & Terlevich 1996; Cristiani et al. 1996; Cristiani, Trentini, La Franca, & Andreani 1997; Paltani & Courvoisier 1997; Giveon et al. 1999; Garcia, Sodr , Jablonski, & Terlevich 1999; Hawkins 2000; Webb & Malkan 2000). Such an anti-correlation is expected in Poissonian models, although complex versions are necessary to explain the diversity of the relationship among quasars (Cid Fernandes, Sodr , & Vieira da Silva 2000).

There is strong evidence from multiwavelength observations of quasars that variability increases with decreasing rest wavelength, which holds over a wavelength range spanning at least the ultraviolet to near infrared (Cutri, Wisniewski, Rieke, & Lebofsky 1985; Neugebauer, Soifer, Matthews, & Elias 1989; Kinney, Bohlin, Blades, & York 1991; Paltani & Courvoisier 1994; di Clemente et al. 1996; Cristiani, Trentini, La Franca, & Andreani 1997; Giveon et al. 1999; Cid Fernandes, Sodr , & Vieira da Silva 2000; Helfand et al. 2001; Trèvese & Vagnetti 2002). The wavelength dependence is related to the observed tendency for quasar spectra to become harder (bluer) in bright phases (Cutri, Wisniewski, Rieke, & Lebofsky 1985; Edelson, Pike, & Krolik 1990; Giveon et al. 1999; Cid Fernandes, Sodr , & Vieira da Silva 2000; Trèvese, Kron, & Bunone 2001). The chromatic nature of quasar variability is often taken as evidence against gravitational microlensing as the primary cause of variability (e.g. Cristiani, Trentini, La Franca, & Andreani (1997); except see Hawkins (1996)), although this may be accounted for if regions closer to the center are both brighter and bluer.

A correlation of variability with redshift is often reported (Cristiani, Vio, & Andreani 1990; Giallongo, Trevese, & Vagnetti 1991; Hook, McMahon, Boyle, & Irwin 1994; Trèvese et al. 1994; Cid Fernandes, Aretxaga, & Terlevich 1996; Cristiani et al. 1996; Trèvese & Vagnetti 2002) if wavelength and luminosity dependencies are not taken into account. For a fixed observer timescale, the increase of variability with increasing redshift would contradict the expected $1 + z$ effect of time dilation.

However, it has been shown by Giallongo, Trevese, & Vagnetti (1991), Cristiani et al. (1996), and Cid Fernandes, Aretxaga, & Terlevich (1996) that the inverse wavelength dependence can easily account for the uncorrected redshift correlation, since for a fixed passband in the observer frame, quasars with higher redshifts are detected at shorter wavelengths, which systematically vary at a greater amplitude. It is still not clear whether any redshift dependence remains after accounting for rest wavelength and luminosity (which is strongly correlated with redshift in flux-limited quasar samples). Some studies which have leverage in both redshift and luminosity suggest a weak correlation of redshift and variability (Hook, McMahon, Boyle, & Irwin 1994; Cristiani et al. 1996), but others show no such effect (Cimatti, Zamorani, & Marano 1993; Paltani & Courvoisier 1994; Netzer et al. 1996; Cristiani, Trentini, La Franca, & Andreani 1997; Helfand et al. 2001).

Variability is sometimes found to be correlated with radio loudness (Pica & Smith 1983; Smith & Nair 1995; Garcia, Sodr , Jablonski, & Terlevich 1999; Eggers, Shaffer, & Weistrop 2000; Helfand et al. 2001; Enya et al. 2002), the equivalent width of the $H\beta$ line (Giveon et al. 1999; Cid Fernandes, Sodr , & Vieira da Silva 2000), and the presence of broad absorption line troughs (Sirola et al. 1998), although the results are not conclusive. No large X-ray detected quasar sample has been systematically studied for optical variability, but since most blazars are X-ray bright, a greater degree of variability may be expected from such a sample (e.g. Ulrich, Maraschi, & Urry 1997).

In this paper we present results on a quasar variability program using data from the Sloan Digital Sky Survey (SDSS, York et al. 2000). A complementary variability study by de Vries, Becker, & White (2003) presents a comparison of the SDSS Early Data Release (Stoughton et al. 2002) imaging photometry with archival photographic plate data. One of the goals of the present work is to characterize the spectroscopic calibrations of the SDSS, in order to examine the spectroscopic variability properties of quasars and other objects observed in the spectroscopic survey. The present work uses the broad band fluxes of the spectra convolved with the SDSS filter transmission functions in direct comparison with the imaging photometry. This provides photometric data at two

epochs in three bands for every spectroscopically confirmed quasar in the survey – a sample size currently of over 25000 quasars. This is by far the largest quasar UV/optical variability study to date, and it also includes the largest samples of radio selected, X-ray selected, and broad absorption line quasars ever examined for variability. Our goal is to characterize the ensemble dependence of variability on many quasar parameters and types, on timescales from weeks up to several years.

We describe the quasar sample drawn from the SDSS in § 2. Ensemble measurements of the variability are given in § 3. We disentangle the dependence of variability upon time lag, luminosity, wavelength, and redshift in § 4, show how quasar colors change with variability in § 5, and look at variability in various quasar subclasses in § 6. The implications of the results are discussed in § 7, and we conclude in § 8. Throughout the paper we assume a flat, cosmological constant dominated cosmology with parameter values $\Omega_\Lambda = 0.7$, $\Omega_M = 0.3$, and $H_0 = 65\text{km/s/Mpc}$.

2. The Quasar Dataset

2.1. The Sloan Digital Sky Survey

The Sloan Digital Sky Survey (SDSS) is a project to image 10^4 deg^2 of sky mainly in the northern Galactic cap, in five broad photometric bands (u, g, r, i, z) to a depth of $r \sim 23$, and to obtain spectra of 10^6 galaxies and 10^5 quasars observed in the imaging survey (York et al. 2000). All observations are made with a dedicated 2.5m telescope at Apache Point Observatory in New Mexico. Images are taken with a large mosaic CCD camera (Gunn et al. 1998) in a drift-scanning mode. Absolute astrometry for point sources is accurate to better than 100 milliarcseconds (Pier et al. 2003). Site photometricity and extinction monitoring are carried out simultaneously with a dedicated 20in telescope at the observing site (Hogg, Finkbeiner, Schlegel, & Gunn 2001). The imaging data are reduced and calibrated using the PHOTO software pipeline (Lupton et al. 2001). In this study we use the point-spread function (PSF) magnitudes, which are determined by convolving the reduced imaging data with a model of the spatial point-spread function. The PSF magnitudes are more stable than aperture magnitudes for point sources, since they are less dependent

upon seeing variations, and because the PSF background noise is less within the survey seeing limit (which is 1.7 arcseconds). The SDSS photometric system is normalized so that the u, g, r, i, z magnitudes are on the AB system (Smith et al. 2002; Fukugita et al. 1996; Oke & Gunn 1983). The photometric zeropoint calibration is accurate to better than 1% (root-mean-squared) in the g, r , and i , bands, and to better than 2% in the u and z bands, measured by comparing the photometry of objects in scan overlap regions. The SDSS image reduction and calibration routines have evolved throughout the course of the survey and the imaging runs have been reprocessed accordingly. Thus the object imaging magnitudes deemed “best”, and which we use in this study, may be slightly different than those used for the spectroscopic target selection, although any differences are insignificant to the results of this study. Throughout this paper we use magnitudes corrected for Galactic extinction according to Schlegel, Finkbeiner, & Davis (1998).

Objects are selected for spectroscopic follow-up as candidate galaxies (Strauss et al. 2002; Eisenstein et al. 2001), quasars (Richards et al. 2002), and stars (Stoughton et al. 2002). The spectroscopic targets are grouped by 3 degree diameter areas or “tiles” (Blanton et al. 2003). For each tile, an aluminum plate is drilled with holes corresponding to the sky locations of the targets along with holes for blank sky, calibration stars, and guide stars. The plates are placed at the focal plane of the telescope, and optical fibers run from the hole positions to two spectrographs, each of which accepts 320 fibers allowing for the simultaneous observation of 640 objects. For each plate, approximately 500 galaxies, 50 quasars, and 50 stars are observed. Spectroscopic observations generally occur up to a few months, but occasionally years, after the corresponding imaging observations, depending upon scheduling constraints. The spectroscopic data for this study come from 479 spectroscopic plates observed and processed through September 2002; 284 of the plates are part of the SDSS First Data Release (DR1, Abazajian et al. 2003), publicly available since April 2003. Seven of the (291) DR1 plates are not included in this study, since the DR1 plate list was not finalized until after the sample for this study had been gathered.

2.2. Quasar Target Selection and Sample Definition

Quasar candidates are selected from the imaging sample by their non-stellar colors from the five-band photometry as well as by matching SDSS point sources with FIRST radio sources (Stoughton et al. 2002). The selection is similar to that described by Richards et al. (2002), but the formal implementation of this algorithm was imposed after the cutoff date for the DR1 quasar sample, and much of the post-DR1 data used in this study. About two-thirds of the candidates are confirmed to be quasars from the spectroscopic survey. Ultraviolet excess quasars are targeted to a limit of $i = 19.1$ and higher redshift quasars are targeted to $i = 20.2$. These criteria give a sample that is estimated to be over 90% complete (Richards et al. 2002). Additional quasars are targeted as part of the SERENDIPITY and ROSAT classes (Stoughton et al. 2002) or (incorrectly) as stars.

Quasars are identified from their spectra using a combination of both automated classification (about 94%) and manual inspection (about 6%) of those objects flagged by the spectroscopic pipeline as being less reliably identified. For the purposes of this study, we define “quasar” to mean any extragalactic object with broad emission lines (pipeline measured full width at half maximum velocity width of $\gtrsim 1000\text{kms}^{-1}$) regardless of luminosity. The definition thus includes objects which are often classified as less luminous types of active galactic nuclei (AGNs) rather than quasars, and excludes AGNs without strong broad emission lines such as BL Lacs and some extreme broad absorption line quasars. To assemble our sample, we extract relevant data for all point sources from the SDSS database. Data from only one imaging and one spectroscopic epoch are used per object to avoid giving extra weight to any object. Extended sources are rejected because they complicate the spectrophotometric recalibration (§ 2.4), and their spectra are likely to be seriously contaminated by host galaxy light. Objects with bad spectra (defined to be those with significantly long unprocessable portions of spectrum) are rejected. Those remaining objects spectroscopically identified as stars are used to refine the spectroscopic calibration (see § 2.4). The remaining 25710 objects identified to be quasars become part of the

quasar variability sample.

A catalog of quasars found in the SDSS DR1 dataset is described by Schneider et al. (2003). Of the 16713 listed DR1 quasars, 14705 are included in this study. The difference can be attributed to two factors. First, the definitions of “quasar” are slightly different – Schneider et al. (2003) impose an absolute magnitude limit of $M_i \leq -22.0$, and they make no distinction between point-like and extended sources. Second, data from only 284 of the 291 DR1 spectroscopic plates are included in this study. Over half (57%) of the quasars in this study are contained in the DR1 sample, and we expect that our results on quasar variability would be similar (albeit more noisy) for the full DR1 sample, except possibly for the extended sources.

Absolute magnitudes in the rest frame i band M_i , are calculated for each quasar using dereddened observed i band PSF magnitudes and assuming a power law spectral energy distribution $f_\lambda \propto \lambda^{\alpha_\lambda}$, with a wavelength slope of $\alpha_\lambda = -1.5$. Detailed K-corrections are not yet available for quasars in the SDSS photometric system. However, estimated K-corrections using the composite spectrum from Vanden Berk et al. (2001) are consistent with the simple power law assumption, and the differences are usually no greater than 0.1 magnitude at any redshift. The differences are not significant here since the data are coarsely binned (by statistical necessity) when we examine absolute magnitude trends.

2.3. SDSS Spectroscopy and Its Calibration

Spectra are obtained in three to four consecutive 15-minute observations. There are 32 sky fibers, 8 spectrophotometric standard stars and 8 reddening standards stars observed on each plate to help with calibration of the remaining 592 science targets. Spectral reductions and calibrations are done using the SDSS SPECTRO 2D pipeline (Stoughton et al. 2002). The 8 spectrophotometric calibration stars are chosen to approximate the standard F0 subdwarf star $BD+17^\circ4708$, and are used by the 2D pipeline for absolute spectral flux calibration and dereddening due to Galactic extinction. The 2D pipeline also calculates synthetic spectroscopic magnitudes by convolving the calibrated spectra with SDSS g , r , and i filter transmission curves, assuming 1.2 airmasses of extinc-

tion (the spectra do not cover the entire wavelength ranges of the u and z bands). By using these synthetic spectral magnitudes, we obtain a second photometric data point for every spectroscopically observed quasar. Additionally, a signal-to-noise (S/N) parameter is calculated for each of the three bands by convolving the spectral error with the transmission curves and dividing that into the corresponding convolved flux. The spectral magnitude signal-to-noise is essential for characterizing magnitude difference uncertainties (see §2.4).

2.4. Refinement of Spectroscopic Calibration

The differences between the spectroscopic and imaging PSF magnitudes $\Delta m = m_s - m_p$ for all of the spectroscopically confirmed stars in each of the g , r , and i bands are shown in Fig. 1. Well calibrated data should center around zero magnitude difference, and there should be no trend with magnitude, except for larger uncertainties at fainter magnitudes. There are clearly systematic differences in the magnitudes derived from the spectra and from the images. While the initial spectroscopic calibration is more than adequate for the primary purposes of the SDSS, namely object identification and reliable redshift measurement, variability studies require more careful calibrations. Fortunately, the magnitude difference trends with PSF magnitude can be easily understood and are almost entirely correctable.

There are three primary sources for the magnitude difference discrepancy: the inclusion of objects with bad PSF magnitudes, an aperture effect relating the finite fiber diameters to the PSF magnitudes, and what may be a very small but significant sky under-subtraction in the spectroscopic data. Occasionally, point sources in the images can have poor photometry if they are closely blended with other objects, occur where the seeing has changed very rapidly, or lie where there may be other problems in the imaging data. The long tails in the histograms of Fig. 1 are populated mainly by the measurements of these objects. Because the objects will have unusual measured colors they are sometimes selected as high-redshift quasar candidates for spectroscopic follow-up, which turn out to be normal stars upon examination of the spectra. Therefore, spectroscopically confirmed stars

which were selected as high-redshift quasar candidates are removed from the stellar data set for spectrophotometric refinement. Late-type stars identified by the spectroscopic pipeline are also rejected because they are often variable.

The median Δm offset from zero is simply an aperture effect wherein the $3''$ spectroscopic fibers subtend a smaller fraction of the total object image than the point-spread function used to measure the PSF magnitudes in the imaging data. The spectroscopic fiber flux density to PSF flux density ratio is nearly a constant (but somewhat dependent upon seeing at the spectroscopic epoch, see below), so the magnitude difference will also be a nearly (non-zero) constant.

The downward trend of Δm with PSF magnitude seen for each band is most easily accounted for by a small overestimation of the flux density in the spectroscopic data, possibly caused by a slight under-subtraction of the sky level. Tests of the imaging photometric calibration show that the effect is not likely to be caused by sky over-subtraction in the imaging data. Further tests will have to be done to determine the cause with certainty. The correction for a flux density overestimation combined with a fiber aperture correction give

$$\begin{aligned}\Delta m &= m_s - m_p = -2.5 \log(f_s/f_p) \\ &= -2.5 \log(a(f_p + b)/f_p) \\ &= -2.5 \log(a + ab10^{(m_p - C)/2.5}) ,\end{aligned}\quad (1)$$

where a is the aperture correction, b is the correction for the flux density offset, and C is the zeropoint constant used in converting flux density to magnitude. Assuming a and b are constants, the function has two adjustable parameters, and fits to the data provide reasonably good descriptions of the Δm vs. m_p trend. However, in order to account for any other effects, expected or unexpected, we use the following more flexible 3 parameter function

$$\Delta m = \Delta m_0 - \exp((m_p - m_0)/m^*) ,\quad (2)$$

where Δm_0 , m_0 , and m^* are constants to be determined from the fits to the data. For example, the Malmquist bias (Malmquist 1924) will add to the magnitude difference approximately as the square of the PSF magnitude uncertainty, σ_p^2 . Since σ_p ranges from about 0.01 to 0.05, the Malmquist bias

is expected to affect the magnitude difference by at most a few percent. In the absence of this or other higher order effects, the 3-parameter function would almost exactly reproduce the 2 parameter logarithmic fit. The 3-parameter functions are fit to the data in each band separately, then subtracted from the magnitude differences.

After this correction, offsets from zero remain for the mean Δm values for stars on the same plate, in excess of those expected from statistical uncertainty. These plate-to-plate offsets are due to differences in the spectral energy distributions of the stars used as initial spectrophotometric calibrators relative to $BD + 17^\circ 4708$ and due to differences in the seeing at the epochs of the plate observations. The former effect applies to “half plates” corresponding to the two sets of 320 fibers running separately to each spectrograph. To correct for these effects, we reject stars outside of the 99% confidence envelope resulting from the Δm corrections described above, and work only with half plates which have at least 5 remaining stars (the average number is about 20). The median Δm offsets are calculated for each half plate and subtracted from the values for each of the stars observed with that half plate.

The final corrected Δm distributions are shown in Fig. 2 as a function of spectral S/N . The width of the stellar Δm distribution is correlated with magnitude, but the better correlation is with spectral S/N . The reason for this is that while magnitude and S/N are correlated, it is the S/N which is directly related to the quality of a spectrum. As a whole, the 68.3% confidence half-width (nominally 1 standard deviation) is ≈ 0.08 in each band at a spectroscopic S/N of 10, which is a substantial improvement over the initial widths of ≈ 0.13 . Fits to the 68.3% confidence half-width as a function of spectral S/N are shown in Fig. 2, for which we used a function of the form

$$\sigma_{S/N} = a_0 + a_1 \exp(a_2 S/N) ,\quad (3)$$

where a_0 , a_1 , and a_2 are constants. These fits are used as statistical measurement uncertainties for the quasars (see § 3).

The same spectrophotometric corrections applied to the stars are also applied to the quasars. The resulting distribution of quasar magnitude differences as a function of spectral S/N , and the histograms of magnitude differences are shown in

Fig. 3. The mean corrected magnitude differences for the quasars are 0.002, -0.004, and -0.011 for the g , r , and i bands respectively. These values are small compared with the measurement uncertainties derived from the stars. It is possible that small differences in the spectral energy distributions (SEDs) of stars and quasars affect the recalibration of the quasar photometry. However, any effect is expected to be quite small since the same filter transmission curves are used for both the imaging and spectroscopic photometry, and the majority of the stars used for the recalibration were selected as quasar candidates in the color-selected survey, which guarantees that the SEDs are very similar. The 68.3% confidence limit half-widths of the g , r , and i magnitude difference distributions are 0.134, 0.119, and 0.114 respectively at a S/N of 10, substantially larger than those of the stars. The stars and quasars were selected to be point sources, observed simultaneously with the same instrument, and often were selected with the same algorithm. The larger magnitude differences among the quasars, therefore, demonstrate the variable nature of the quasars in the sample. The following sections quantify the variability and its dependence upon many quasar parameters.

3. Ensemble Variability Measurement – The Structure Function

The magnitude difference histograms from the previous section show that the quasars are significantly more variable as a class than the stars. Assuming no stellar variability, we can use the distribution of the stellar magnitude differences to quantify the statistical measurement uncertainties. Removing the width of the stellar magnitude difference distribution in quadrature, the average quasar magnitude differences (at a spectral S/N of 10) due to variability in the sample are 0.103, 0.086, and 0.080 in the g , r , and i bands respectively. Measurement uncertainties must be taken into account because they are comparable to the values of the variability itself. The large sizes of the samples (both the quasars and the comparison stars) allow the measurement uncertainty to be effectively removed.

We first show the absolute values of the measured quasar magnitude variations, uncorrected for measurement uncertainty, in Figures 4 through

7, as a function of quasar rest frame time lag (Fig. 4), absolute magnitude in the rest frame i band (Fig. 5), rest frame wavelength (Fig. 6), and redshift (Fig. 7). Data in each of the three photometric bands are shown separately. Average values in a set of bins are also shown. Because flux densities in the $\text{Ly}\alpha$ forest region are not representative of the true quasar flux, we have omitted data in each band at redshifts beyond which the $\text{Ly}\alpha$ forest covers the band: $z = 2.5$, 4.75, and 6.0 for the g , r , and i bands respectively. The number of measurements rejected for each band due to the $\text{Ly}\alpha$ forest are 742, 45, and 0 for the g , r , and i band respectively. The figures show that there are several apparent correlations even in the uncorrected data. In particular, the average magnitude difference increases with time lag in all three bands, and the magnitude difference decreases with more negative absolute magnitude (decreases with luminosity). No trends are apparent at this stage between magnitude difference and rest wavelength or redshift. Again, it is important to account for measurement uncertainty before making any claims about the dependence of variability on any parameter.

The definition of variability used here is a statistical measure of the magnitude difference, taking into account measurement uncertainty. The first application is to the dependence of variability on rest frame time lag – the so-called structure function. Historically, the structure function has been the primary measure of variability for studies of both individual quasars and quasar ensembles. For individual quasars with multiple sampling epochs, the structure function is comprised of the values of the magnitude differences for each pair of time lags in the data set, and it is closely related to the autocorrelation function (e.g. Simonetti, Cordes, & Heeschen 1985). In the ensemble case, here with only two sampling epochs, the structure function is simply the average value of the magnitude difference for all objects with the same (or nearly the same) time lags. The error analysis is simpler in the ensemble case since all of the data points are independent.

We define the ensemble variability, V , of a set of quasars as

$$V = \left(\frac{\pi}{2} \langle |\Delta m|^2 \rangle - \langle \sigma_{S/N}^2 \rangle \right)^{\frac{1}{2}}, \quad (4)$$

where Δm is the measured magnitude difference, $\sigma_{S/N}$ is the statistical measurement uncertainty of Δm (as a function of spectral S/N) derived from the fits to the star measurements in §2.4, and the brackets denote average quantities. The average absolute value of the magnitude difference, along with the scaling factor of $\pi/2$, is more robust against the presence of outliers in the data than the average of the square of the differences. The values V as a function of rest frame time lag $\Delta\tau$, define the structure function, $V(\Delta\tau)$. The same relation has been used for the structure function in previous variability studies (e.g. di Clemente et al. 1996).

The binned structure function for all of the quasars in the sample for each of the three photometric bands is shown in Fig. 8 with logarithmic axes. The bins were chosen to have equal intervals in logarithmic rest frame time lag, and to have reasonably large numbers of objects. The number of objects per bin range from 241 for the shortest time lag bin covering 7 to 11 days in the g band, to 7919 for the i band bin covering time lags from 111 to 176 days. Quasars with magnitude differences larger than 0.75 – just over 5 times the 1σ width of the distribution for quasars – were rejected from the analysis in order to remove outliers. This step removes about 1% of the quasars, which is more than would be expected for a truly normal distribution. In a related paper (Ivezić et al. 2003), the distribution of ultraviolet-excess quasar magnitude differences, including very large differences, is discussed in more detail. The apparently highly variable quasars may be optically violent variables and are valuable for follow-up studies, but the focus here is on “typical” quasar variability. The error bars were determined by propagating the root-mean-square errors σ^2 , in the average magnitude difference and measurement uncertainty in quadrature

$$\sigma(V) = \frac{1}{2}V^{-1}\sqrt{\pi^2\langle|\Delta m|^2\rangle^2\sigma^2(\langle|\Delta m|\rangle) + \sigma^2(\langle\sigma_{S/N}^2\rangle)} . \quad (5)$$

Two trends are obvious: first the structure function increases as a function of time lag – the magnitude differences are greater the longer the time between measurements. Second, the amplitude of variability is greater in the g (bluest) band than in the others, and the r band amplitude is generally greater than in the i (reddest) band. This is the variability anticorrelation with wavelength found

in a several previous studies. We will quantify the wavelength dependence explicitly in §4.4, accounting for the dependence on other parameters. For the purposes of the remainder of this section, the clear wavelength dependence means that the analysis of the structure function will address the three bands individually.

The correlation of variability with time lag has been found in numerous previous studies, however the form of the structure function has remained a topic of debate. We fit the binned structure functions with the two most common parameterizations. The first is a power law (e.g. Hook, McMahon, Boyle, & Irwin 1994)

$$V(\Delta\tau) = \left(\frac{\Delta\tau}{\Delta\tau_0}\right)^\gamma , \quad (6)$$

where $\Delta\tau_0$ and γ are constant parameters to be determined. This will appear as a straight line in a log-log plot such as Fig. 8. The second is an asymptotic function – a constant minus an exponential – which is the most common parameterization of the structure function (e.g. Bonoli et al. 1979; Trèvese et al. 1994; Hook, McMahon, Boyle, & Irwin 1994; Enya et al. 2002)

$$V(\Delta\tau) = V_0 \left(1 - e^{-\frac{\Delta\tau}{\Delta\tau_0}}\right) , \quad (7)$$

where again V_0 and $\Delta\tau_0$ are to be determined. The “time scales”, $\Delta\tau_0$, whatever their values, are simply parameters of the functions to be fit to the data, and can not necessarily be directly compared with physical characteristic time scales, such as those associated with accretion disks, star bursts, or gravitational lens dynamics.

Parameter values, uncertainties, and χ^2 values for each of the functions in each of the photometric bands are given in Table 1. Based on the χ^2 values, the functional form that best fits the structure function in each band is a power law. The power law slopes in each of the three bands for g , r , and i respectively – are consistent with each other within one standard deviation of the difference. The power law scale factors (where the structure functions would have a value of one) are not well constrained, mainly because the observed time lag only extends to about 700 days. The shape of the structure function at much longer time lags is sometimes observed to “flatten” somewhat (Cristiani, Trentini, La Franca, & Andreani

(1997); Hook, McMahon, Boyle, & Irwin (1994); Trèvese et al. (1994); see Hawkins (2002) for a counter-example), but the data at long time lags do not yet favor one parameterization over another. In any case, what we can say from this study is that a 2-parameter power law is a good description of the data – and a better description than a 2-parameter exponential – up to time lags of about 2 years. As the SDSS proceeds, the range of time lags will eventually reach up to about 5 years. The rest frame time sampling will continue to improve on all scales, and the power law form can be even more stringently tested on longer time scales.

The wavelength dependence of the structure function becomes clearer at longer time lags (and should become even clearer by survey end), as would be expected from either a power law or exponential fit. The distributions of quasar properties – e.g. luminosity and rest frame wavelength – vary with rest frame time lag because of survey selection effects and the dependence of these properties on redshift. In the next section we disentangle the dependence of variability on four primary quasar parameters.

4. Variability Dependence on Time Lag, Luminosity, Wavelength, and Redshift

4.1. Selection Function

The structure function calculated in the previous section describes the variability of the full data set with respect to time lag. However, variability is almost certainly also a function of quasar luminosity and rest frame wavelength, and possibly redshift. In order to separate the dependence of variability on multiple parameters, the selection biases must be taken into account. Even the structure function may not give the true dependence of variability on rest frame time lag. The set of quasars within a narrow range of time lags will be populated with objects with wide ranges of the other parameters. In addition, since rest frame time lag is dependent upon redshift, as are the other parameters, the distributions of quasar parameter values will be correlated with the time lag. For example, high redshift quasars will generally have shorter time lags in the rest frame than lower redshift quasars.

The selection function – that is, the region of

parameter space occupied by the data set – is shown in projected planes in Fig. 9. A number of artificial correlations are evident and are due both to the survey selection criteria, and to the dependence of luminosity, rest frame time lag, and rest wavelength on redshift. Variability information can obviously only be obtained in the regions of the four dimensional parameter space containing a statistically sufficient number of objects.

In order to determine how variability is related to a single parameter, the space was divided into small regions in three dimensions, and the variability calculated as a function of the remaining parameter in each of the slices. The condition that there be enough quasars to reliably measure variability was the primary limiting factor for the bin sizes. For each parameter there is then a set of variability relations, each set representing the results of restricting the ranges of the other 3-parameters. As shown in the remainder of this section, in most cases variability trends are clear even in independent restricted data sets.

If we make the assumption that the equations describing the multi-parameter dependence of variability are separable, the results from each of the slices may be scaled in the single parameter ranges where they overlap, in order to find the variability dependence upon a single parameter. That is, the form of the variability dependence is assumed to be

$$V(\Delta\tau, M_i, \lambda, z) = v(\Delta\tau) \times v(M_i) \times v(\lambda) \times v(z) \quad , \quad (8)$$

where V is calculated as in the previous section. While this form is not necessarily correct, it greatly simplifies the analysis, and the relatively simple relations found for each parameter suggest that it is not far from reality. In the following subsections, we show the unscaled variability relations for single parameters in the independent restricted data sets, then show the results after scaling the independent sets together assuming equation 8. The scaled relations are fit with relatively simple descriptive functions for each parameter.

4.2. Time Lag

We focus first on the dependence of variability on rest frame time lag, independent of the other 3 parameters. The full quasar sample was first separated into 6 redshift bins, each with an equal

spacing in logarithmic $1 + z$. The redshift bin sides are: 0.185, 0.499, 0.895, 1.395, 2.028, 2.829, and 3.840. The quasar sample in each redshift bin was then divided into two halves separated at the median absolute magnitude of the quasars in the redshift bin: $M_{i,median} = -22.96, -24.07, -25.24, -26.07, -26.73, \text{ and } -27.09$. Taking each photometric band separately for the quasars in each of the 12 redshift/absolute magnitude bins restricted the quasar rest wavelengths to small ranges. The procedure produced 36 independent data sets confined to small ranges of redshift, absolute magnitude, and rest wavelength, but unrestricted with respect to rest frame time lag. The variability amplitude and uncertainty as a function of time lag were determined as in §3, for the quasars in each of the 36 data sets independently. The time lag bins were set to have a constant logarithmic time width, as in §3, but with twice the width to accommodate the smaller number of objects per bin. The rest frame time lag bin sides, in days, are: 7.0, 17.6, 44.3, 111.1, 278.7, and 699.2. Unphysical (imaginary) values of the variability amplitude occurred in a small number (3) of cases in which the number of quasars was relatively small. In most cases when this occurs the number of quasars is 5 or fewer. For all further analysis, binned data sets containing fewer than 10 quasars or which produce imaginary values of the variability amplitude are rejected. For each of the 36 data sets, the variability with respect to rest frame time lag is an independent structure function over which the absolute magnitude, rest wavelength, and redshift do not vary greatly. The results are shown in Fig. 10. Results for the three photometric bands, corresponding to restricted ranges of rest wavelength, are shown in separate panels. The average redshift of the quasars contributing to each structure function is indicated by color, with redder colors representing progressively higher redshifts. The structure functions containing the more luminous halves of the quasar data sets are shown with solid points, and the less luminous halves with open points.

It is clear from Fig. 10 that variability is an increasing function of rest frame time lag at all redshifts, absolute magnitudes, and rest wavelengths. Two other trends can also be seen: the less luminous quasars vary more than their more luminous counterparts (nearly all of the open points

lie above the solid points within the same redshift bin); and quasars vary more at shorter wavelengths, confirming what was shown by the unrestricted structure functions in §3.

Under the assumption that the variability as a function of time lag is separable from the other dependencies, the individual structure functions can be scaled together in the time lag regions where they overlap. Using as a reference a structure function near the middle of the redshift, luminosity, and wavelength distributions, all 36 structure functions (excluding bins with too few objects) were scaled such that the sum of the products of the amplitudes and the time lag bin widths (the areas under the curves) were equal. The scaled points are shown in the last panel of Fig. 10 along with the best fit power law. The parameter fits to a power law and exponential are given in Table 2. A 2-parameter power law provides a very good fit and is better than the asymptotic (exponential) form. The power law fit has a slope of $\gamma = 0.246 \pm 0.008$, which is comparable to but shallower than the values found for the unrestricted structure functions in §3. Scaling the data points will change the characteristic time scale of the function (the time lag at which the power law amplitude would be unity), but not the power law slope. That the slope is relatively close to those found for the unrestricted structure functions is due to the offsetting variability dependencies on luminosity and rest wavelength. From Fig. 9, longer time lags are statistically populated by more luminous objects, which vary less, but at shorter wavelengths, where the variability is greater. The significance of the power law slope in relation to variability models is discussed in §7.

4.3. Absolute Magnitude

The luminosity (absolute magnitude) dependence of variability is separated from the other parameters in a similar way to the time lag in the previous subsection. The full quasar sample was separated into the same 6 redshift bins, and each separate quasar sample was further divided into two halves at the median rest frame time lag of the quasars in the redshift bin. The median rest frame time lags, in days, for each redshift bin are: 249.9, 192.0, 157.1, 122.9, 100.5, and 73.6. Again considering the three photometric bands separately restricted the rest wavelengths of each data set

to small ranges. This produced 36 independent quasar subsamples unrestricted with respect to absolute magnitude. The variability amplitude as a function of absolute magnitude, in bins one magnitude in width, is shown for each quasar subsample in Fig. 11. The variability amplitude is an increasing function of absolute magnitude (brighter objects vary less) for nearly every subsample. Also seen in Fig. 11 are the time lag dependence – variability amplitudes are greater at longer time lags (filled symbols) than short time lags (open symbols) – and a wavelength dependence, seen most easily in the amplitude differences between the g and i bands. This is a clear demonstration that the well-known luminosity-variability anticorrelation is not simply due to time lag or rest wavelength selection effects.

The data sets were again scaled such that that the areas under the curves were equal. In each redshift bin, the six individual sets (3 wavelength and 2 time lag bins) were scaled to have identical sums of the product of the absolute magnitude bin width and variability amplitude. Then proceeding from the lowest to highest redshifts, the scaled redshift sets were rescaled to the adjacent redshift set so that the areas under the curves were equal in regions where the absolute magnitude coverage overlapped. The scaled data points are shown in the last panel of Fig. 11. A straight line can be fit to the data points, but such a description is unphysical since at large luminosities (large negative absolute magnitudes) the function becomes negative. In so called Poissonian or discrete-events models the relative luminosity variability, $\delta L/L$ is expected to vary with luminosity as $\delta L/L \propto L^{-\beta}$, where $\beta = \frac{1}{2}$ in general (e.g. Cid Fernandes, Sodré, & Vieira da Silva 2000). This relationship translates into the absolute magnitude form

$$v(M_i) \propto 10^{\beta M_i/2.5} . \quad (9)$$

This function and one in which β is held fixed at 0.5 were fit to the data. Both fits are shown in Fig. 11. The logarithmic equation, with a best fit of $\beta = 0.246 \pm 0.005$, fits the data as well as a straight line, and avoids the problem of negative values. The Poissonian prediction of $\beta = 0.5$ gives a poor fit and is clearly inconsistent with the data. Scaling the individual data sets, which accounts for arbitrary contributions from variability dependencies on time lag, rest wavelength, and redshift,

does not change the value of β . We will discuss the implications for Poissonian models further in §7.

4.4. Rest Wavelength

The rest wavelength dependence of variability was isolated for subsamples selected to cover small ranges in redshift, time lag, and absolute magnitude. The redshift and absolute magnitude bins are the same ones used to isolate the time lag dependence (12 separate bins, see §4.2). The data in each of these bins were divided into three separate samples in the plane of absolute magnitude and time lag, according to the following lines: $M_i = 0.085\Delta\tau - 31.25$ and $M_i = 0.024\Delta\tau - 31.42$. This gives 36 independent data sets covering small ranges of redshift, absolute magnitude, and time lag. All but one of the data sets contain enough objects to compute reliable variability measurements. Each data set samples three separate rest wavelength points given by the effective rest wavelengths of the three photometric bands. The variability amplitude as a function of the rest frame wavelength for each set is shown in Fig. 12. The average rest frame time lag in each set is color coded (longer time lags are redder), the more luminous half of a redshift/time lag bin is shown with solid points, and each redshift subset is shown in a separate panel.

In most cases, the variability amplitude decreases with wavelength as expected from previous analysis. The cases in which the opposite happens occur at short time lags and very low or very high redshifts, but there are too few cases to make any claims about deviations from the general trend. The time lag and luminosity dependencies are also evident from the figure.

The data points were scaled in a manner similar to that in §4.3. For each redshift bin, the six sets of points (3 time lag bins and 2 absolute magnitude bins) were scaled to the same area under the curves and then, moving from low to high redshift, the points were rescaled to match the appropriate area in the adjacent redshift bin. In this case, since the rest wavelength bin limits are not equal for the separate redshift bins, the three wavelength points in each set were connected by two straight lines, and the area under the lines was calculated in the regions where they overlapped the wavelengths of the adjacent redshift bin points. The

scaled points as a function of rest wavelength are shown in Fig. 13. If the variability is due to a simple change in the index of a single power law, we would expect the wavelength dependence to be

$$v(\lambda) = -2.5\Delta\alpha_\lambda \log(\lambda) + C, \quad (10)$$

where $\Delta\alpha_\lambda$ is the difference in the wavelength power law index, and C is a constant related to the pivot wavelength (where the two power laws intersect) presumed to be much longer than the observed wavelengths. Figure 13 is plotted with a logarithmic wavelength axis, and so the relation would be seen as a straight line. A single straight line is an adequate fit from the shortest wavelengths up to about 4000\AA , but does not account well for the longer wavelength end. Contamination from host galaxy light at longer wavelengths would have the opposite effect – cause the variability to decrease even faster with wavelength. A 3-parameter exponential function, although physically unmotivated, fits the data well

$$v(\lambda) = a_0 \exp(-\lambda/\lambda_0) + a_1, \quad (11)$$

with parameter values $a_0 = 0.616 \pm 0.056$, $\lambda_0 = 988 \pm 60\text{\AA}$, and $a_1 = 0.164 \pm 0.003$.

4.5. Redshift

The redshift dependence of variability is more difficult to isolate from the time lag, absolute magnitude, and wavelength dependencies. The reason for this can be seen from inspection of Fig. 9. For example, samples restricted to a narrow range of rest wavelengths will have 3 independent redshift intervals (taking the three bands separately), but the corresponding absolute magnitude ranges for the redshift intervals may not overlap appreciably. So to isolate the redshift dependence, we first found a region of wavelength-absolute magnitude space which is covered by quasar data in all three bands. Fig. 14 shows the wavelength-absolute magnitude plane and the selected region which is bounded by a triangle with corners $(\lambda, M_i) : (1250, -27.0), (1250, -29.4), \text{ and } (3491, -23.8)$. Outside of this region quasar data are generally available for only 2 or fewer of the bands. The data contained in this region were then separated into 16 wavelength bins, shown in Fig. 14, at intervals of 100, 200, 400, or 800\AA , depending on the number of objects contained in

the bin. For each bin of wavelength separated data, objects were selected from a single range of time lags chosen so that the average absolute magnitudes, time lags, and wavelengths were about equal for data in each of the three photometric bands. Taking each of the photometric bands separately for a restricted data set gives a wide range of redshifts, while keeping the ranges of time lag, absolute magnitude, and rest wavelength nearly constant.

The variability amplitudes for all 16 data sets (each with three redshift points) are shown in Fig. 15. The number of objects contributing to each point ranges from 65 to 1150, with a mean number of 239. Lines connect the points belonging to data sets with nearly the same parameter values but at different redshifts. The color of the points and lines corresponds to the average absolute magnitude of the data set, with bluer colors representing brighter absolute magnitudes. The point sizes correspond to the average time lag of the objects contributing to the points. The absolute magnitude correlation, discussed above, is evident in Fig. 15, but it is partly counteracted by the nearly monotonically increasing rest wavelength with average absolute magnitude (seen from Fig. 14), and the generally longer average time lags associated with fainter average absolute magnitudes.

What is of interest here is the dependence of the variability on redshift. The results are fairly noisy and it is difficult to detect any clear trend with redshift. The sets of points were scaled by matching the areas under the curves of adjacent data sets, as in the previous subsections, starting with the sample with the shortest rest wavelengths. The scaled data points are shown in Fig. 16. There is a correlation between the scaled variability and redshift – quasars appear to be more variable at higher redshifts. The Spearman rank correlation probability that the points are uncorrelated is less than 10^{-4} , even after accounting for the reduction of the number degrees of freedom by the number of restricted data sets (16). A straight line fit to the data points (linear in redshift and variability amplitude) gives

$$v(z) = (0.019 \pm 0.002)z + (0.037 \pm 0.005). \quad (12)$$

The correlation, although significant, is weak enough that it could easily have gone unnoticed in previous variability studies, especially since most

of them suffer from a lack of sufficient sample overlap needed to test the redshift relationship independently of other parameters. The redshift evolution of variability would have serious consequences for a number of currently proposed models. If the effect is intrinsic, the quasar population or the variability mechanism is changing over time. External causes are also possible, such as gravitational microlensing which may increase with redshift since more potential lenses would be available. The variability correlation with redshift is discussed further in §7.

5. Color Dependence

Evidence from previous ensemble studies (Trèvese, Kron, & Bunone 2001; Giveon et al. 1999; Edelson, Pike, & Krolik 1990) suggests that the spectral energy distribution of quasars becomes harder (bluer) in bright phases. Indirect evidence also comes from the fact that there is a strong wavelength dependence upon variability (§4.4). This could happen for example if the index of a power law component of the continuum changes with luminosity (Trèvese & Vagnetti 2002).

Quasar colors are a strong function of redshift (Richards et al. 2001), since various spectral features move into and out of the photometric bandpasses with redshift changes. A pure power law spectrum would have a single set of colors independent of redshift. The observed quasar color structure is mainly due to the presence of strong emission features, especially broad Fe II complexes, as well as the Ly α forest. Figure 17 shows the average imaging photometric colors of quasars as a function of redshift in two samples selected to be either brighter or fainter by at least 3 standard deviations in at least one of the g, r, i bands relative to the spectrophotometry. We use the imaging photometric colors rather than the spectroscopic since they are more precise, and two more colors are available. Although the color differences are small (~ 0.03), at most redshifts up to at least 2.5 and for each color the bright phase sample is bluer than the faint phase sample. Also shown in Fig. 17 are the color differences of the bright phase minus the faint phase samples as a function of redshift. Both the binned and average color differences are shown. The color differences are increasingly larger for shorter wavelength bands,

i.e. quasars in bright phases are bluer than those in faint phases, and they are even bluer at shorter wavelengths.

That the color change persists at high redshift also indicates that it cannot be accounted for solely by a non-variable red spectral component, such as the quasar host galaxy. Such a component would contribute a higher fraction of the total quasar light in the faint phases, making quasars appear redder than in the bright phases. Any reasonable host galaxy spectral energy distribution and luminosity would contribute very little light to the bluest bands, and would quickly be redshifted out of the other bands. By a redshift of 0.5, there should be almost no significant contamination from the host galaxies in any of the passbands. A host galaxy component cannot account for the wide range of redshifts over which the color difference is significant.

6. Variability of Radio, X-ray, and Broad Absorption Line Quasars

There is evidence from previous studies that the variability amplitude of quasars varies among different subclasses, such as those with radio emission (Helfand et al. 2001; Eggers, Shaffer, & Weistrop 2000; Garcia, Sodré, Jablonski, & Terlevich 1999; Pica & Smith 1983) or broad absorption line systems (Sirolo et al. 1998). The entire class of highly variable blazars, for example, is defined in part by X-ray and radio emission (e.g. Ulrich, Maraschi, & Urry 1997). Here we examine the variability of broad subclasses of quasars in comparison to carefully selected control samples.

6.1. Radio Detected Quasars

Some SDSS quasar candidates are selected as optical matches to radio sources in the FIRST survey (White, Becker, Helfand, & Gregg 1997; Ivezić et al. 2002). About 10% of the verified quasars in the sample have counterparts in the FIRST survey. In the areas of the SDSS sample covered by the FIRST survey at the time the quasar candidates were selected, there are 1553 verified quasars with FIRST catalog matches. To test whether quasars with detected radio emission are more or less variable than those without, we have extracted a control sample of quasars without matches in the FIRST catalog. The non-radio-detected control

sample was constructed to have the same redshift, luminosity, and time lag distribution as the radio-detected sample, by matching each radio quasar with a non-radio quasar with nearly the same redshift, magnitude, and time lag. The standard deviations of the redshift, magnitude, and time lag differences are $\sigma(\Delta z) = 0.03$, $\sigma(\Delta m) = 0.04$ mag., and $\sigma(\Delta(\Delta\tau)) = 3.6$ days, and in no case were the differences allowed to be greater than 0.5, 0.5 mag., and 40 days respectively. Of the FIRST matched quasars, 1376, 1389, and 1388 were able to be matched with counterparts in the non-FIRST sample in the g , r , and i bands respectively. Kolmogorov-Smirnov tests comparing the redshift, magnitude, and time lag distributions of the radio and control samples show that they are statistically indistinguishable. This also guarantees that the wavelength coverages of the samples are nearly identical.

A radio-loud (not simply radio-detected) sub-sample and its corresponding non-radio control sample were also generated. Radio loudness is defined here as the ratio of the rest frame 5GHz to 4500Å flux-densities (e.g. Sramek & Weedman 1980), and a quasar is deemed radio-loud if the ratio is at least 100. The sample sizes of the radio-loud quasars and the matched radio-quiet control quasars are 492, 530, and 546 objects for the g , r , and i bands respectively.

The matched time lag structure functions for the full radio and non-radio samples are shown in Fig. 18. There is no significant difference in the binned structure functions of the radio-detected and undetected quasars. On the other hand, the matched structure functions for the radio-loud sub-sample, shown in Fig. 19, are about 1.3 times higher than the non-radio sample. However, only the difference in the i band is significant (matched pair t -test probability of 1% if the samples were not truly different). Thus, there is marginal evidence that radio-loud quasars are more optically variable than radio-quiet quasars, but a larger sample will be needed to confirm this.

The qualitative result that the radio-loud quasars are more variable agrees with most of the past suggestions (Helfand et al. 2001; Eggers, Shaffer, & Weistrop 2000; Garcia, Sodr , Jablonski, & Terlevich 1999; Pica & Smith 1983). Since most blazars are radio-loud (e.g. Ulrich, Maraschi, & Urry 1997), the higher variability amplitude

of radio-loud quasars may reflect a higher fraction of blazars. There is not enough information from this survey to reliably classify individual objects as blazars (at the very least, more detailed lightcurves are needed). Further subdivision of the sample by finer radio loudness currently yields too few quasars for meaningful comparisons. In any case, the evidence for a correlation between radio loudness and UV/optical variability amplitude is suggestive, but not conclusive.

6.2. X-Ray Detected Quasars

As with radio quasars, some of the SDSS quasars are selected for spectroscopic follow-up as matches to sources in the Rosat All Sky Survey (RASS, Voges et al. 1999, 2000). A detailed analysis of RASS source matches to the SDSS data is given by Anderson et al. (2003). About 5% of the verified quasars can be matched with RASS sources, giving about 1300 X-ray quasars in our sample. We constructed the X-ray and control samples in the same way as for the radio sample and its control. The numbers of matched objects in each of the g , r , and i bands are 1010, 1008, and 1009 respectively. Again, Kolmogorov-Smirnov tests show that with respect to redshift, luminosity, and time lag, the two sets of samples are indistinguishable.

The time lag structure functions for the X-ray detected and X-ray-non-detected sample are shown in Fig. 20. The X-ray sample is more variable than the non-X-ray control sample at time lags up to about 250 days, after which the differences of variability amplitudes are much smaller. Overall the X-ray sample amplitudes are larger by a factor of $\approx 10\%$. The matched pair t -test probabilities of the differences occurring by chance are 9.1%, 0.8%, and 0.4% for the g , r , and i bands respectively. The data therefore show that X-ray selected quasars are significantly more variable than their X-ray-non-detected counterparts. However, the difference may become less significant at longer time lags and at longer wavelengths.

The higher X-ray variability amplitude is probably not surprising given the high fraction of X-ray detected objects among blazars. As for the radio sample, the X-ray sample was selected purely by optical matches to catalog sources; no information about the variability of the objects in the sample was used beforehand. This is the first time that a

large X-ray selected sample of quasars has been examined for UV/optical variability. The SDSS sample will soon be large enough to subdivide it further by X-ray brightness. In the meantime, a correlation between X-ray emission and UV/optical variability amplitude can be claimed. We discuss this further in § 7.

6.3. Broad Absorption Line Quasars

Broad absorption line quasars (BALQSOs) are defined by the presence of very strong, blue-shifted absorption troughs in their spectra. About 5% of the quasars in the SDSS sample can be classified as BALQSOs, a fraction which is heavily redshift and color dependent. The largest systematically selected samples of BALQSOs are those of Reichard et al. (2003) and Tolea, Krolik, & Tsvetanov (2002), each of which contain close to the same sets of objects drawn (in somewhat different ways) from the SDSS Early Data Release quasar sample. Both sets contain about 200 objects, and for the present purposes the samples are indistinguishable; we have used the Reichard et al. (2003) sample since the selection process is more automated and is likely to be used for future BALQSO catalogs. A control sample of non-BAL quasars was designed to have consistent redshift, luminosity, and time lag distributions, in the manner described above. The matched sample of BALQSOs contains 178, 189, and 190 objects in the g , r , and i bands respectively.

The matched structure functions are shown in Fig. 21. The time lag binning is necessarily coarse due to the relatively small sample sizes. At the level of sensitivity of this sample, there is no difference in the variability amplitudes of BAL and non-BAL quasars. Currently favored models of the BAL phenomena attribute the absorption to high opacity gas, either as clouds or flows, usually viewed near the plane of an accretion disk. If the presence of BALs is purely a viewing angle effect, then continuum variability, if due to the central quasar engine is unlikely to be correlated. However, if variability is due to the presence of obscuring dust of varying attenuation crossing the sightline to a quasar, BAL quasars may be expected to be more highly variable at optical and UV wavelengths. The issue will need to be settled with a larger sample, but the current results do not support any correlation between the presence

of BAL features and UV/optical variability.

7. Discussion

To summarize our results, we have separated the dependence of variability on a number of parameters, and found a power law dependence on time lag, anticorrelations with wavelength and luminosity, and a correlation with redshift. All of these relationships have been parameterized. Radio loud and X-ray quasars also appear to be more variable than their quiet counterparts. There is currently no model of quasar continuum variability at optical and UV wavelengths that addresses all of the relationships described here, and until recently, there were virtually no quantitative predictions. Current models can be classified broadly into three groups: accretion disk instabilities, discrete-event or Poissonian processes, and gravitational microlensing. We ignore other evidence for or against the theories and describe how variability as an independent phenomenon may constrain the models.

The Poissonian models postulate that quasar luminosity, or at least a significant fraction of it, is generated by some type of multiple discrete and independent energetic events, such as supernovae or star collisions (e.g. Terlevich, Tenorio-Tagle, Franco, & Melnick 1992; Torricelli-Ciamponi, Foellmi, Courvoisier, & Paltani 2000). The statistical superposition of the light curves of the randomly occurring events determines the luminosity at any given time. As discussed in § 4.3, the simplest Poissonian models predict a luminosity dependent power law slope of $\beta = 1/2$ which is inconsistent with our results. More detailed models in which the event rate, energy, timescale, and background contribution are adjustable parameters can produce a wide range of slopes (Cid Fernandes, Sodré, & Vieira da Silva 2000), but a value of $\beta = 1/2$ is still difficult to avoid in models invoking supernovae and their remnants as the events (Paltani & Courvoisier 1997; Aretxaga, Cid Fernandes, & Terlevich 1997). Another apparently unavoidable consequence of the Poissonian models is that the variable luminosity component is not wavelength dependent (Cid Fernandes, Sodré, & Vieira da Silva 2000), and any color changes must be the result of a non-variable component (such as a host galaxy), which must be red to qualitatively

account for the wavelength correlation found here and in other studies. We have shown that the variable source itself is wavelength dependent, and a host galaxy component alone cannot account for the color changes. Quantitative predictions for the power law slope of the structure function in the starburst (supernova) model (Kawaguchi, Mineshige, Umemura, & Turner 1998) range from $\gamma \approx 0.7 - 0.9$, which are also quite inconsistent with the value we find ($\gamma = 0.246$). Thus, based on predictions for the time lag, wavelength, and luminosity dependence of variability, current Poissonian models are inconsistent with the observational results of this study. It remains to be seen if non-Poissonian processes, for example in which the events are not independent or random, can account for the observations.

The idea that the motions of intervening matter along the geodesics to quasars may cause flux variations (microlensing) was discussed as early as the late 1970s (Chang & Refsdal 1979), but few quantitative predictions have been worked out with regard to typical quasar variability. Using the simulated microlensing light curves of Lewis, Miralda-Escude, Richardson, & Wambsganss (1993) and Schneider & Weiss (1987), Hawkins (2002) generated structure functions which have a power law form with slopes ranging from $\gamma \approx 0.23$ to $\gamma \approx 0.31$ (Hawkins 2002), which is consistent with what we find. However, the slopes depend upon the unknown lens mass distribution function, velocity distribution, and source size (Wyithe & Turner 2001), so that a wide range of values is possible. There is little doubt that microlensing of quasar images does happen, and it has likely been detected in at least two cases, Q2237+0305 (Schmidt et al. 2002, and references therein) and Q0957+561 (Refsdal, Stabell, Pelt, & Schild 2000). However in each case, the quasar is *macrolensed* by a foreground galaxy, which means that the geodesics selectively pass through regions of relatively high density. Wyithe & Turner (2002) showed that the probability of microlensing by stars among single image (not macrolensed) sources is very small; dark matter composed of compact objects can improve the probability, but at most only about 10% of sources are expected to be microlensed at any given time. In addition, since unresolved macrolensed quasars – which appear more luminous than they really are – are

more likely to be microlensed, the anticorrelation of variability amplitude with luminosity is opposite to the trend that would be expected from microlensing. While the deflection of light by gravity is achromatic, the wavelength dependence of variability is not necessarily evidence against the microlensing hypothesis, as long as quasar emitting regions are smaller and brighter with decreasing wavelength. It is difficult, however, to see why there would be any dependence on the radio or X-ray properties of the quasar sample. The amplitude of quasar variability changes with redshift, but it is nearly as strong at low redshifts as it is at high redshifts, which also shows that microlensing can not be the primary cause of variability, since microlensing events should be extremely rare at low redshift. Finally, reverberation mapping studies (Peterson 2001) show that the quasar broad line region varies in response to changes in the continuum luminosity, showing that a large fraction of variability must be intrinsic to quasars. If some quasar variability is due to microlensing, it will be important to isolate it from the other sources since it has the potential to constrain the components of dark matter and the structure of quasars.

It is widely accepted that quasar luminosity is generated through some set of processes related to the accretion of matter from a disk onto a supermassive black hole (e.g. Rees 1984). It is therefore natural to consider mechanisms associated with changes in these processes as a source of quasar variability. Qualitatively, most schemes would tend to follow the trends we find here, in particular the anticorrelations of variability with wavelength and luminosity. For example, the disk emission spectrum of the standard optically thick geometrically thin accretion disk model (e.g. Shakura & Sunyaev 1973) is more luminous and bluer when the accretion rate is higher, and the relative luminosity change would be lower in more luminous objects for a given change in accretion rate. However, it is not known how the accretion rate would change nor how the resultant luminosity changes would propagate through the disk. While there has been much theoretical discussion of the various possibilities for the emission mechanisms and their instabilities (e.g. Wallinder, Kato, & Abramowicz 1992; Schramkowski & Torkelson 1996), there are currently few quantitative predictions which can be compared to observa-

tional results. Kawaguchi, Mineshige, Umemura, & Turner (1998) generated structure functions for the cellular-automaton model for disk instability, and found power law forms with slopes ranging from $\gamma = 0.41$ to 0.49 . While this range is inconsistent with our results, the model is necessarily simplified and a number of assumptions need to be made. The complexity of possible accretion disk (or jet) instability models is likely what has prevented more quantitative predictions. Disk instability models are clearly promising, but as yet it is difficult to compare them to the observations.

In summary, the weight of the observational evidence seems to disfavor gravitational microlensing and generic Poissonian processes as the primary source of quasar variability. Accretion disk instability models have yet to be adequately developed quantitatively for direct comparison with our results. It is also plausible that a combination of sources produce variations in quasar lightcurves, and no single model can be completely eliminated at this time.

8. Conclusions

We have examined the ensemble broadband photometric variability of a very large and homogeneous sample of quasars from the SDSS – the largest sample ever used to study variability. The three-band spectrophotometry of each object was compared directly to the imaging photometry obtained at an earlier epoch. Because of the large number of objects and wide coverage of parameter space, the dependences of variability amplitude on time lag, luminosity, wavelength, and redshift were able to be disentangled for the first time. The variability amplitude increases with time lag (up to about two years) as a power-law with a slope of $\gamma = 0.25$. In terms of the variability amplitude, more luminous quasars are less variable, shorter wavelengths are more variable, and more distant quasars are somewhat more variable; all of these relationships are parameterized. Radio loud quasars appear to be more variable than their radio quiet counterparts, and quasars with detectable X-ray emission (in the ROSAT survey) are more variable than those without. It is difficult to explain the results in the context of models involving discrete events (Poissonian models) and gravitational microlensing. Accretion disk insta-

bility models are promising, but more quantitative predictions are needed to test them against the observational results.

Funding for the creation and distribution of the SDSS Archive has been provided by the Alfred P. Sloan Foundation, the Participating Institutions, the National Aeronautics and Space Administration, the National Science Foundation, the U.S. Department of Energy, the Japanese Monbukagakusho, and the Max Planck Society. The SDSS Web site is <http://www.sdss.org/>.

The SDSS is managed by the Astrophysical Research Consortium (ARC) for the Participating Institutions. The Participating Institutions are The University of Chicago, Fermilab, the Institute for Advanced Study, the Japan Participation Group, The Johns Hopkins University, Los Alamos National Laboratory, the Max-Planck-Institute for Astronomy (MPIA), the Max-Planck-Institute for Astrophysics (MPA), New Mexico State University, University of Pittsburgh, Princeton University, the United States Naval Observatory, and the University of Washington.

REFERENCES

- Abazajian, K. et al. 2003, AJ, submitted, astro-ph[0305492]
- Anderson, S. F. et al. 2003, AJ, submitted
- Angione, R. J. & Smith, H. J. 1972, IAU Symp. 44: External Galaxies and Quasi-Stellar Objects, 44, 171
- Aretxaga, I., Cid Fernandes, R., & Terlevich, R. J. 1997, MNRAS, 286, 271
- Blanton, M. R., Lin, H., Lupton, R. H., Maley, F. M., Young, N., Zehavi, I., & Loveday, J. 2003, AJ, 125, 2276
- Bonoli, F., Braccisi, A., Federici, L., Zitelli, V., & Formiggini, L. 1979, A&AS, 35, 391
- Chang, K. & Refsdal, S. 1979, Nature, 282, 561
- Cid Fernandes, R. J., Aretxaga, I., & Terlevich, R. 1996, MNRAS, 282, 1191
- Cid Fernandes, R., Sodré, L., & Vieira da Silva, L. 2000, ApJ, 544, 123

- Cimatti, A., Zamorani, G., & Marano, B. 1993, MNRAS, 263, 236
- Collier, S. & Peterson, B. M. 2001, ApJ, 555, 775
- Courvoisier, T. J.-L., Paltani, S., & Walter, R. 1996, A&A, 308, L17
- Cristiani, S., Trentini, S., La Franca, F., Aretxaga, I., Andreani, P., Vio, R., & Gemmo, A. 1996, A&A, 306, 395
- Cristiani, S., Trentini, S., La Franca, F., & Andreani, P. 1997, A&A, 321, 123
- Cristiani, S., Vio, R., & Andreani, P. 1990, AJ, 100, 56
- Cutri, R. M., Wisniewski, W. Z., Rieke, G. H., & Lebofsky, M. J. 1985, ApJ, 296, 423
- de Vries, W. H., Becker, R. H., & White, R. L. 2003, AJ, 126, 1217
- di Clemente, A., Giallongo, E., Natali, G., Trevese, D., & Vagnetti, F. 1996, ApJ, 463, 466
- Edelson, R. A., Pike, G. F., & Krolik, J. H. 1990, ApJ, 359, 86
- Eggers, D., Shaffer, D. B., & Weistrop, D. 2000, AJ, 119, 460
- Eisenstein, D. J. et al. 2001, AJ, 122, 2267
- Enya, K., Yoshii, Y., Kobayashi, Y., Minezaki, T., Suganuma, M., Tomita, H., & Peterson, B. A. 2002, ApJS, 141, 45
- Fukugita, M., Ichikawa, T., Gunn, J. E., Doi, M., Shimasaku, K., & Schneider, D. P. 1996, AJ, 111, 1748
- Garcia, A., Sodré, L., Jablonski, F. J., & Terlevich, R. J. 1999, MNRAS, 309, 803
- Giallongo, E., Trevese, D., & Vagnetti, F. 1991, ApJ, 377, 345
- Giveon, U., Maoz, D., Kaspi, S., Netzer, H., & Smith, P. S. 1999, MNRAS, 306, 637
- Gunn, J. E. et al. 1998, AJ, 116, 3040
- Hawkins, M. R. S. 2002, MNRAS, 329, 76
- Hawkins, M. R. S. 2000, A&AS, 143, 465
- Hawkins, M. R. S. 1996, MNRAS, 278, 787
- Hawkins, M. R. S. 1993, Nature, 366, 242
- Helfand, D. J., Stone, R. P. S., Willman, B., White, R. L., Becker, R. H., Price, T., Gregg, M. D., & McMahon, R. G. 2001, AJ, 121, 1872
- Hogg, D. W., Finkbeiner, D. P., Schlegel, D. J., & Gunn, J. E. 2001, AJ, 122, 2129
- Hook, I. M., McMahon, R. G., Boyle, B. J., & Irwin, M. J. 1994, MNRAS, 268, 305
- Ivezić, Ž. et al. 2002, AJ, 124, 2364
- Ivezić, Ž. 2003, in preparation
- Kawaguchi, T., Mineshige, S., Umemura, M., & Turner, E. L. 1998, ApJ, 504, 671
- Kinney, A. L., Bohlin, R. C., Blades, J. C., & York, D. G. 1991, ApJS, 75, 645
- Lewis, G. F., Miralda-Escude, J., Richardson, D. C., & Wambsganss, J. 1993, MNRAS, 261, 647
- Lloyd, C. 1984, MNRAS, 209, 697
- Lupton, R., Gunn, J. E., Ivezić, Z., Knapp, G. R., Kent, S., & Yasuda, N. 2001, in ASP Conf. Ser. 238, Astronomical Data Analysis Software and Systems X, ed. F. R. Harnden, Jr., F. A. Primini, and H. E. Payne (San Francisco: Astr. Soc. Pac.), p. 269, astro-ph[0101420]
- Malmquist, K. G. 1924, Medd. Lund Astron. Obs., 2(32), 64
- Meusinger, H., Klose, S., Ziener, R., & Scholz, R.-D. 1994, A&A, 289, 67
- Netzer, H. et al. 1996, MNRAS, 279, 429
- Neugebauer, G., Soifer, B. T., Matthews, K., & Elias, J. H. 1989, AJ, 97, 957
- O'Brien, P. T., Gondhalekar, P. M., & Wilson, R. 1988, MNRAS, 233, 845
- Oke, J. B. & Gunn, J. E. 1983, ApJ, 266, 713
- Paltani, S. & Courvoisier, T. J.-L. 1994, A&A, 291, 74
- Paltani, S. & Courvoisier, T. J.-L. 1997, A&A, 323, 717

- Peterson, B. M. 2001, in *Advanced Lectures on the Starburst-AGN Connection*, eds. I. Aretxaga, D. Kunth, & R. Mjica, (Singapore: World Scientific), 3
- Pica, A. J. & Smith, A. G. 1983, *ApJ*, 272, 11
- Pier, J. R., Munn, J. A., Hindsley, R. B., Hennesy, G. S., Kent, S. M., Lupton, R. H., & Ivezić, Ž. 2003, *AJ*, 125, 1559
- Rees, M. J. 1984, *ARA&A*, 22, 471
- Reichard, T. A. et al. 2003, *AJ*, 125, 1711
- Refsdal, S., Stabell, R., Pelt, J., & Schild, R. 2000, *A&A*, 360, 10
- Richards, G. T. et al. 2001, *AJ*, 121, 2308
- Richards, G. T. et al. 2002, *AJ*, 123, 2945
- Schlegel, D. J., Finkbeiner, D. P., & Davis, M. 1998, *ApJ*, 500, 525
- Schmidt, R. W. et al. 2002, *A&A*, 392, 773
- Schneider, D. P. et al. 2003, *AJ*, accepted
- Schneider, P. & Weiss, A. 1987, *A&A*, 171, 49
- Schramkowski, G. P. & Torkelsson, U. 1996, *A&A Rev.*, 7, 55
- Shakura, N. I. & Sunyaev, R. A. 1973, *A&A*, 24, 337
- Simonetti, J. H., Cordes, J. M., & Heeschen, D. S. 1985, *ApJ*, 296, 46
- Sirola, C. J. et al. 1998, *ApJ*, 495, 659
- Smith, A. G. & Nair, A. D. 1995, *PASP*, 107, 863
- Smith, J. A. et al. 2002, *AJ*, 123, 2121
- Sramek, R. A. & Weedman, D. W. 1980, *ApJ*, 238, 435
- Strauss, M. A. et al. 2002, *AJ*, 124, 1810
- Stoughton, C. et al. 2002, *AJ*, 123, 485
- Terlevich, R., Tenorio-Tagle, G., Franco, J., & Melnick, J. 1992, *MNRAS*, 255, 713
- Tolea, A., Krolik, J. H., & Tsvetanov, Z. 2002, *ApJ*, 578, L31
- Torricelli-Ciamponi, G., Foellmi, C., Courvoisier, T. J.-L., & Paltani, S. 2000, *A&A*, 358, 57
- Trèvese, D., Kron, R. G., & Bunone, A. 2001, *ApJ*, 551, 103
- Trèvese, D., Kron, R. G., Majewski, S. R., Bershad, M. A., & Koo, D. C. 1994, *ApJ*, 433, 494
- Trèvese, D. & Vagnetti, F. 2002, *ApJ*, 564, 624
- Ulrich, M., Maraschi, L., & Urry, C. M. 1997, *ARA&A*, 35, 445
- Uomoto, A. K., Wills, B. J., & Wills, D. 1976, *AJ*, 81, 905
- Vanden Berk, D. E. et al. 2001, *AJ*, 122, 549
- Voges, W. et al. 1999, *A&A*, 349, 389
- Voges, W. et al. 2000, *IAUC* 6420
- Wallinder, F. H., Kato, S., & Abramowicz, M. A. 1992, *A&A Rev.*, 4, 79
- White, R. L., Becker, R. H., Helfand, D. J., & Gregg, M. D. 1997, *ApJ*, 475, 479
- Webb, W. & Malkan, M. 2000, *ApJ*, 540, 652
- Wyithe, J. S. B. & Turner, E. L. 2001, *MNRAS*, 320, 21
- Wyithe, J. S. B. & Turner, E. L. 2002, *ApJ*, 575, 650
- York, D. G. et al. 2000, *AJ*, 120, 1579

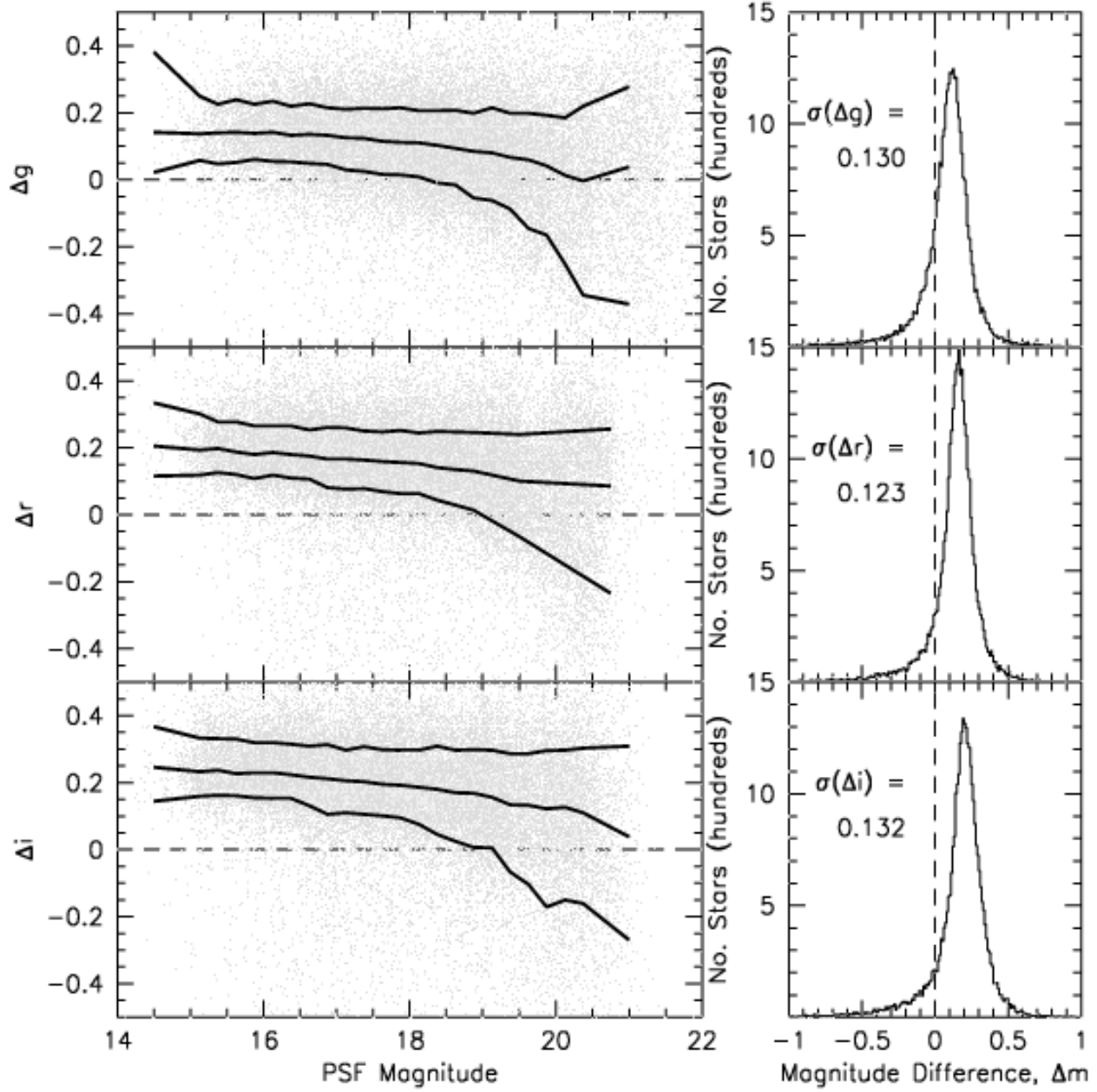


Fig. 1.— The uncorrected spectroscopic minus photometric magnitudes vs. imaging PSF magnitudes for stars observed on the same spectral plates as the quasars (left). Results for all three bandpasses are shown. The curves show the binned median trends and the upper and lower 68.3% confidence envelopes. The right side panels show the uncorrected magnitude difference histograms. The 68.3% confidence half-widths, σ , are given for a spectroscopic S/N of 10.

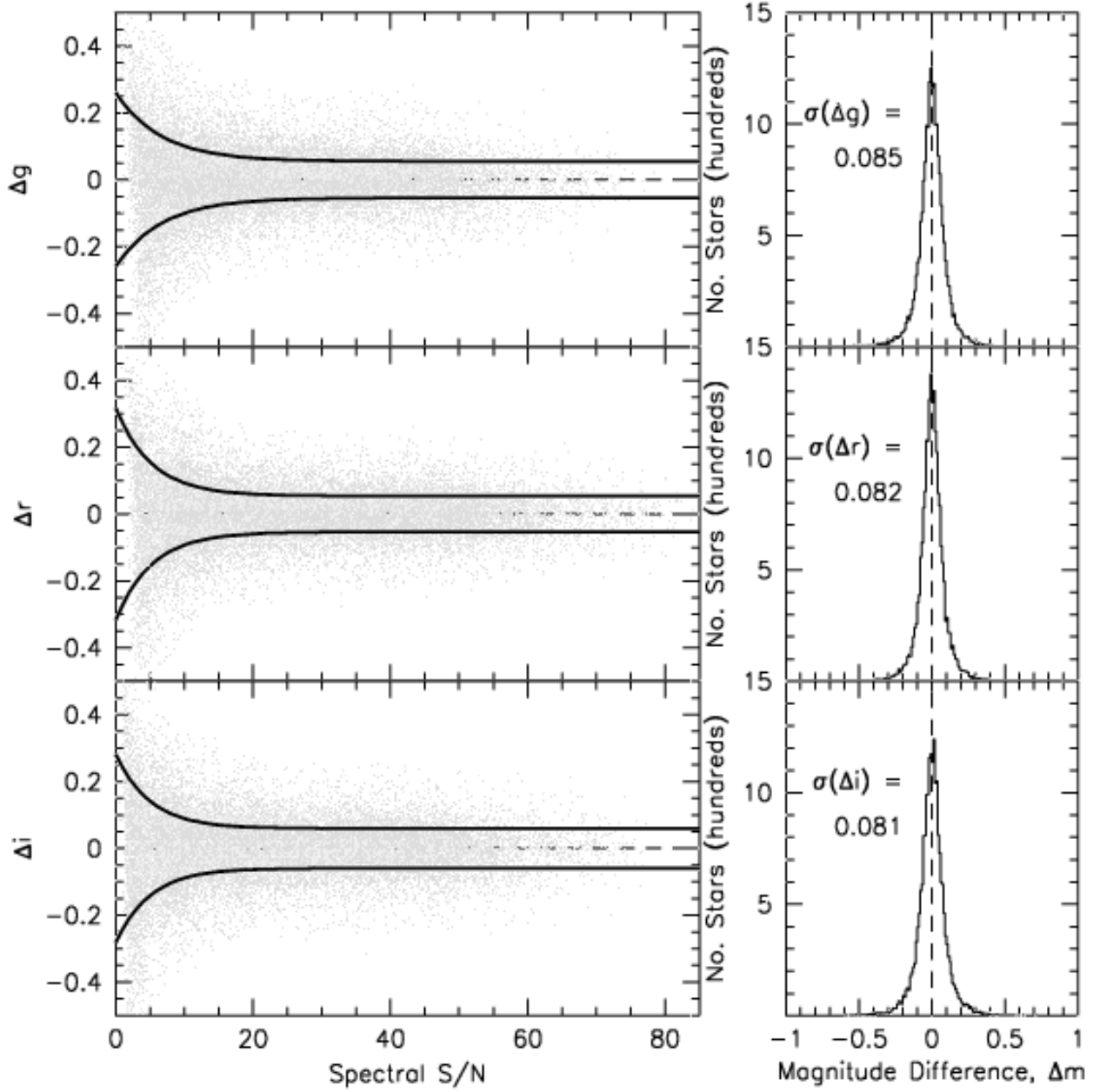


Fig. 2.— The corrected spectroscopic minus photometric magnitudes vs. spectral signal-to-noise ratio for stars observed on the same spectral plates as the quasars (left). Results for all three bandpasses are shown. The curves are the fits to the 68.3% confidence half-width envelopes. The right side panels show the magnitude difference histograms for each band. The 68.3% confidence half-widths, σ are given for a spectroscopic S/N of 10.

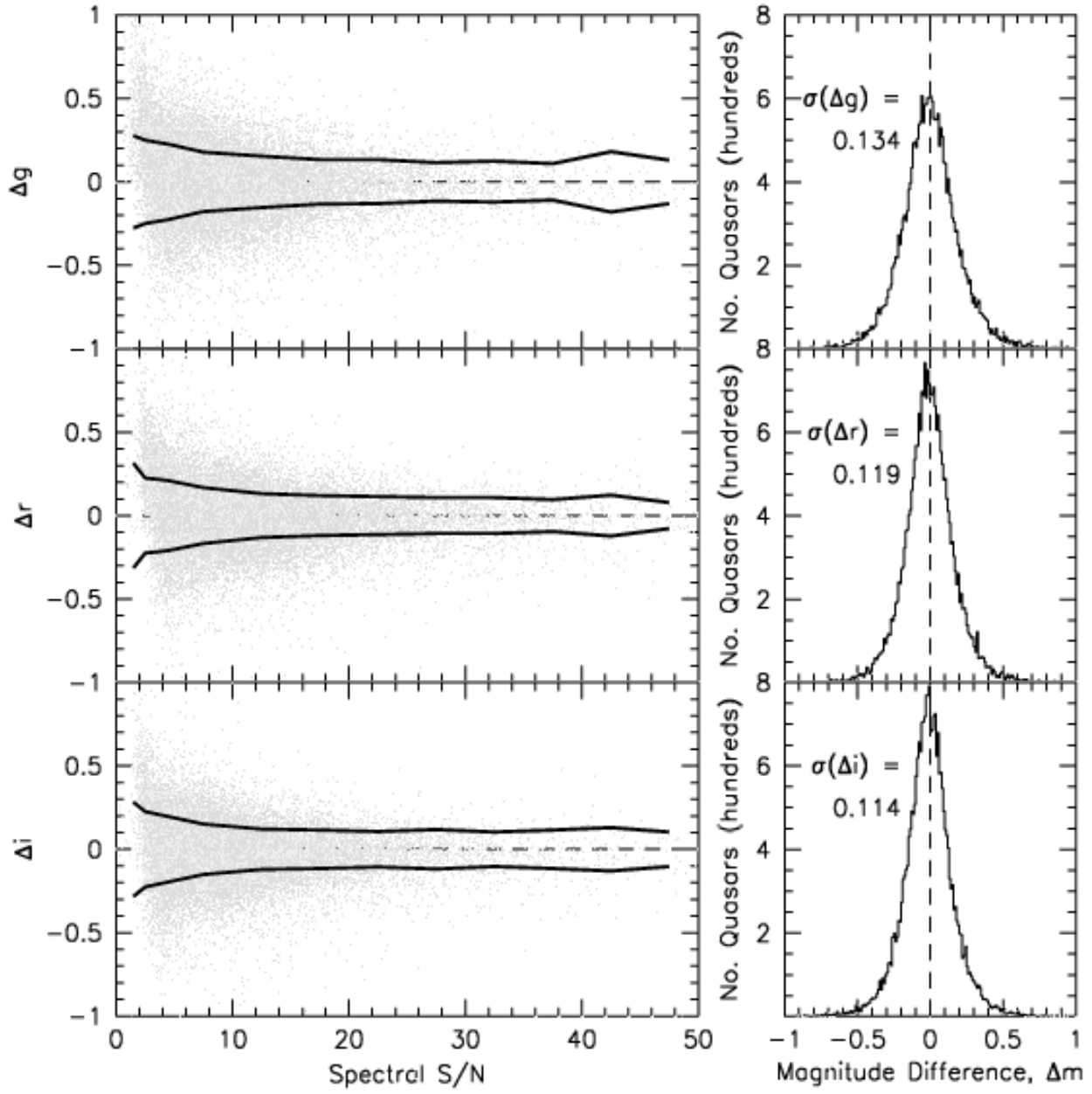


Fig. 3.— The corrected spectroscopic minus photometric magnitudes vs. spectral signal-to-noise ratio for the quasars (left). Results for all three bandpasses are shown. The curves are the binned 68.3% confidence half-width envelopes. The right side panels show the magnitude difference histograms for each band. The 68.3% confidence half-widths, σ , are given for a spectroscopic S/N of 10.

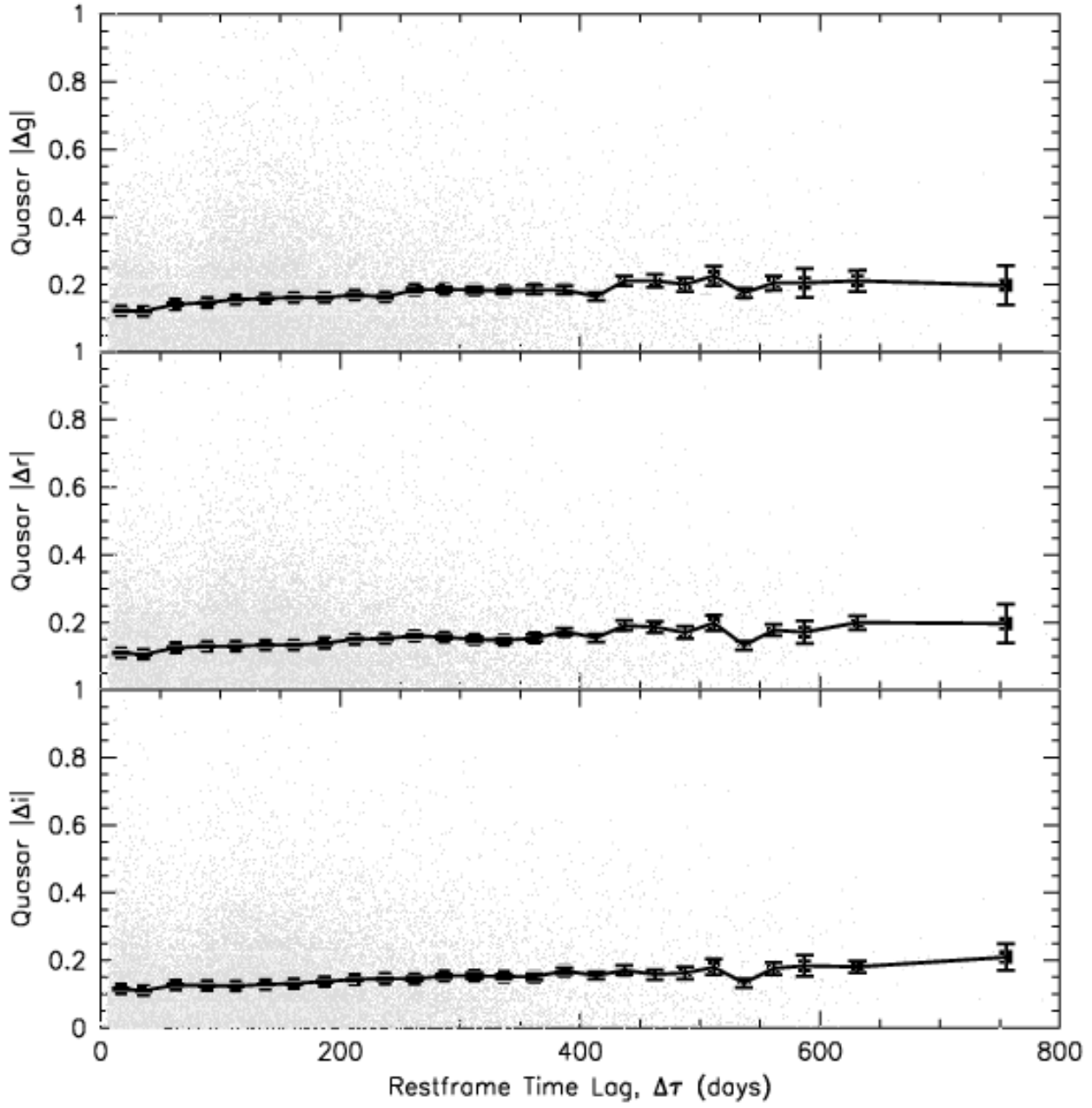


Fig. 4.— Magnitude difference (uncorrected for measurement uncertainties) vs. rest frame time delay in each of the three photometric pass bands. The binned points show the mean values while the error bars show the root-mean-square deviations divided by the square root of the number of objects in a bin.

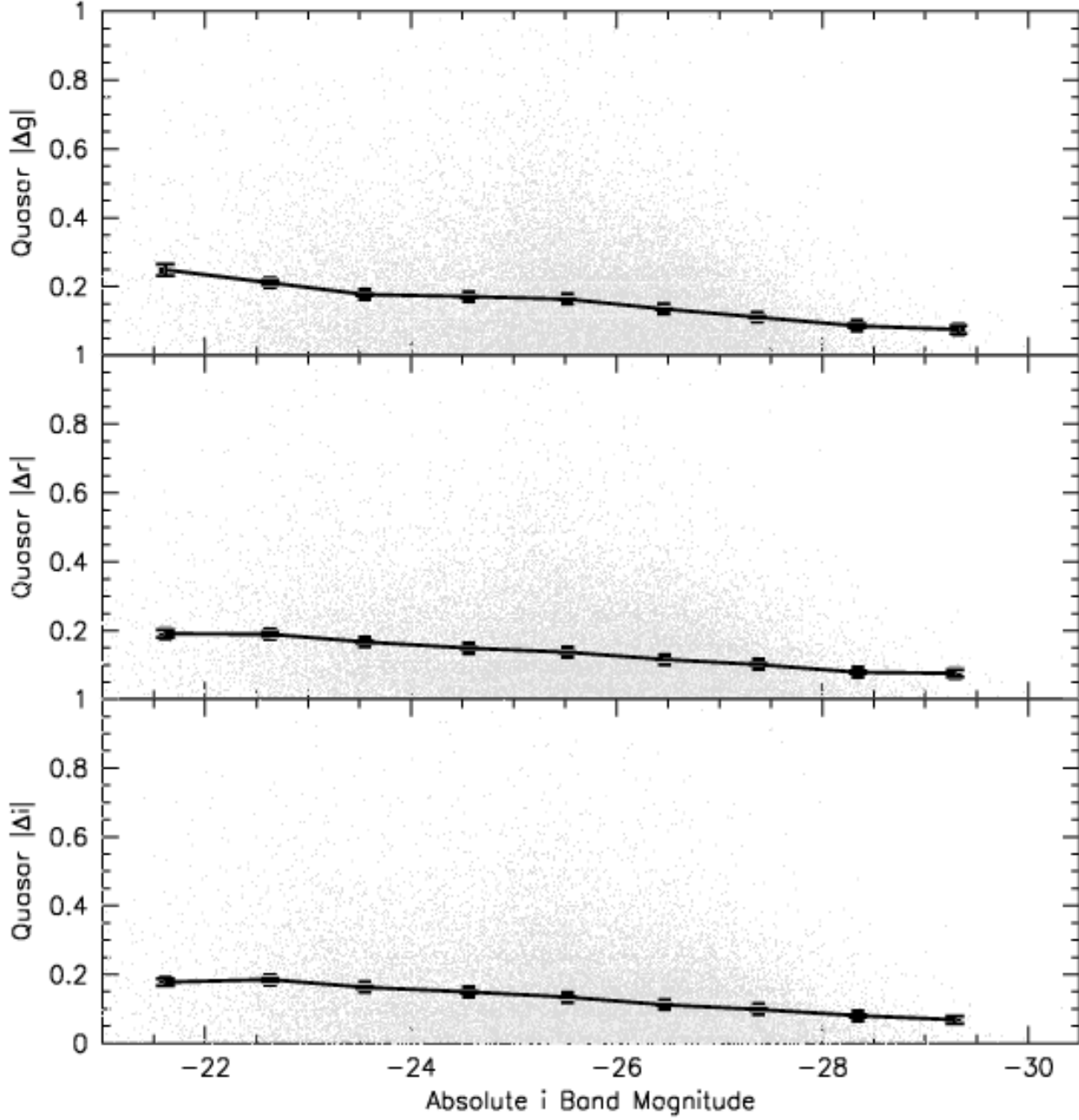


Fig. 5.— Magnitude difference (uncorrected for measurement uncertainties) vs. absolute *i* band magnitude in each of the three photometric pass bands. The binned points show the mean values while the error bars show the root-mean-square deviations divided by the square root of the number of objects in a bin.

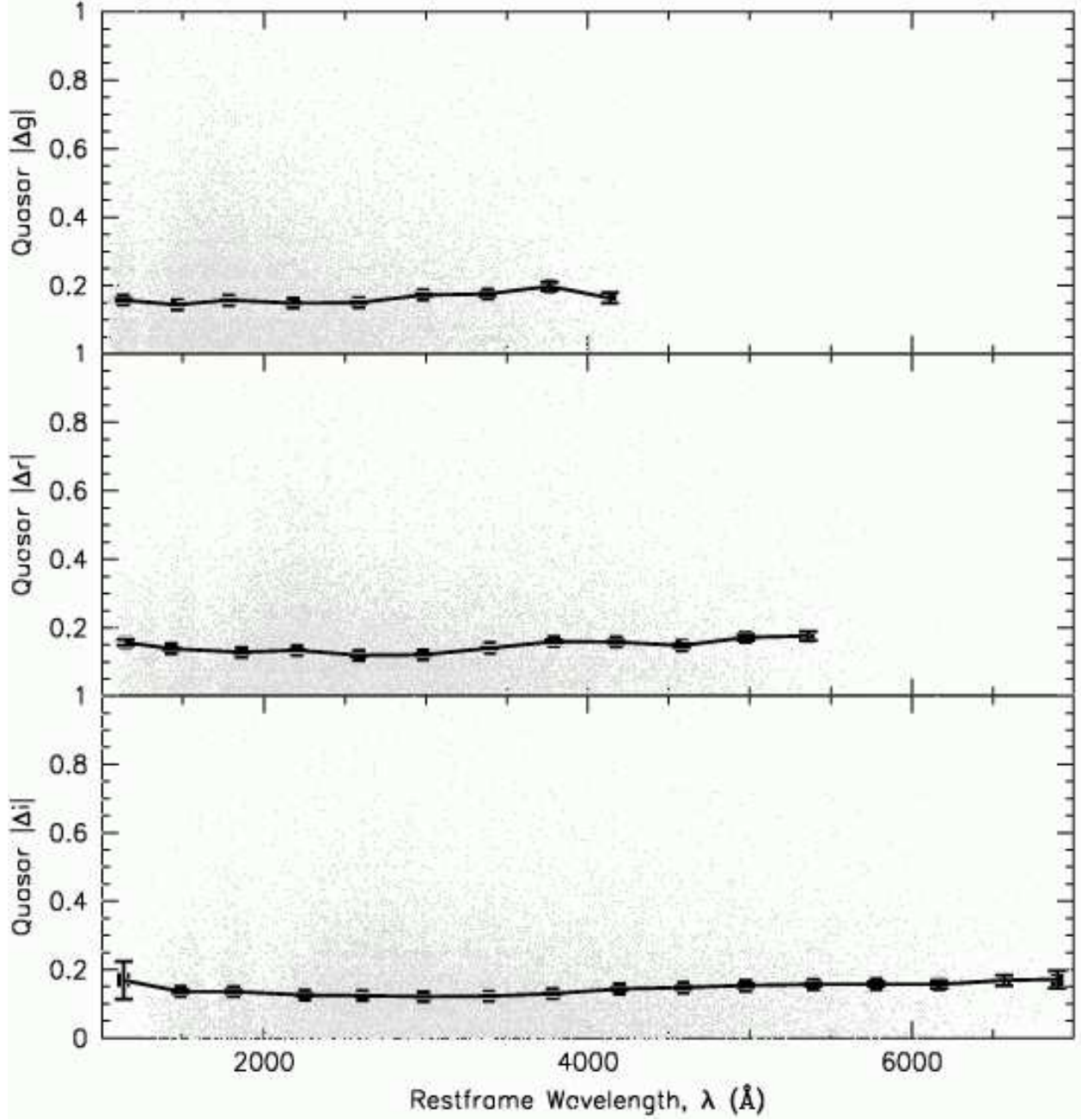


Fig. 6.— Magnitude difference (uncorrected for measurement uncertainties) vs. rest wavelength in each of the three photometric pass bands. The binned points show the mean values while the error bars show the root-mean-square deviations divided by the square root of the number of objects in a bin.

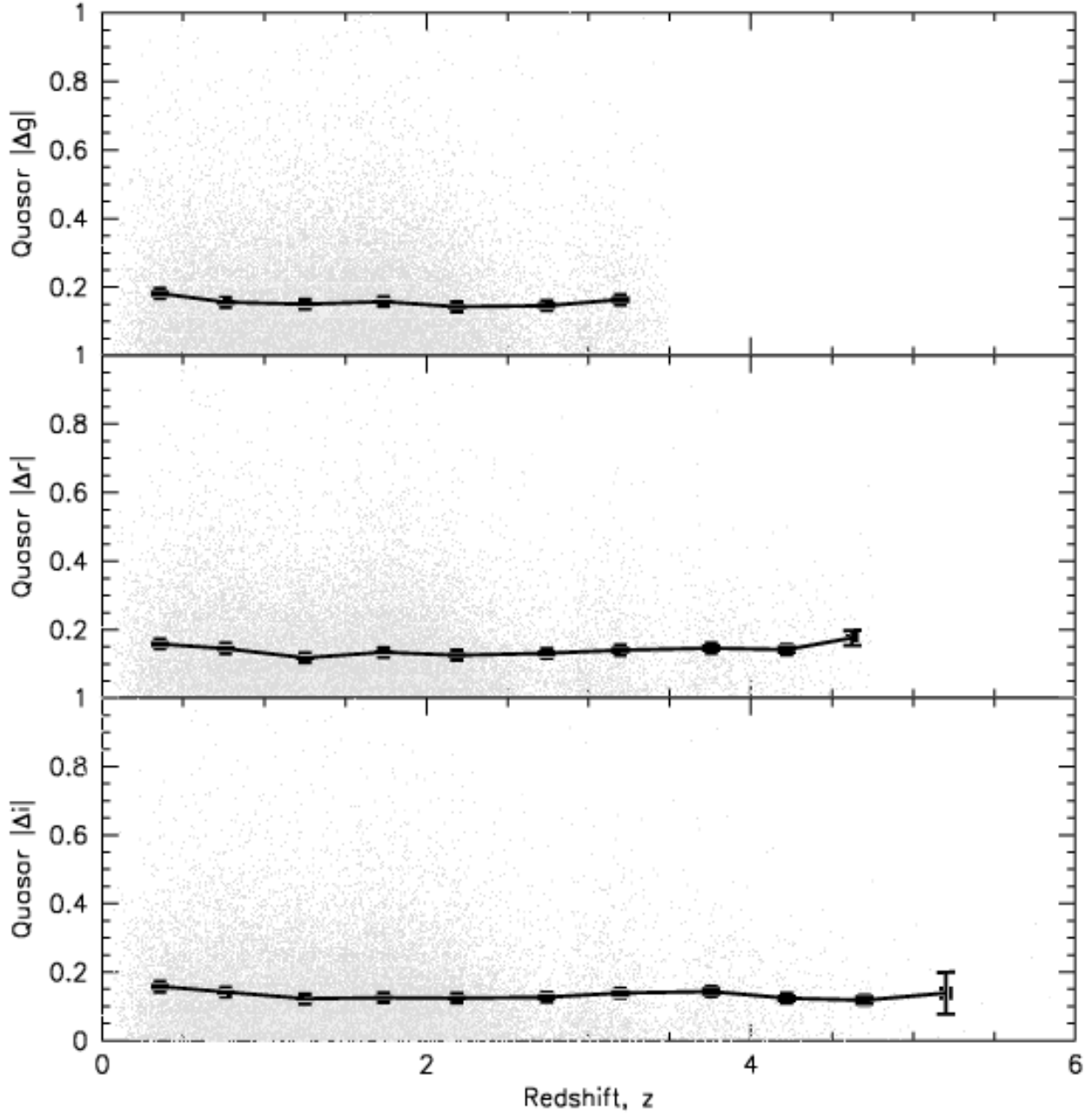


Fig. 7.— Magnitude difference (uncorrected for measurement uncertainties) vs. redshift in each of the three photometric pass bands. The binned points show the mean values while the error bars show the root-mean-square deviations divided by the square root of the number of objects in a bin.

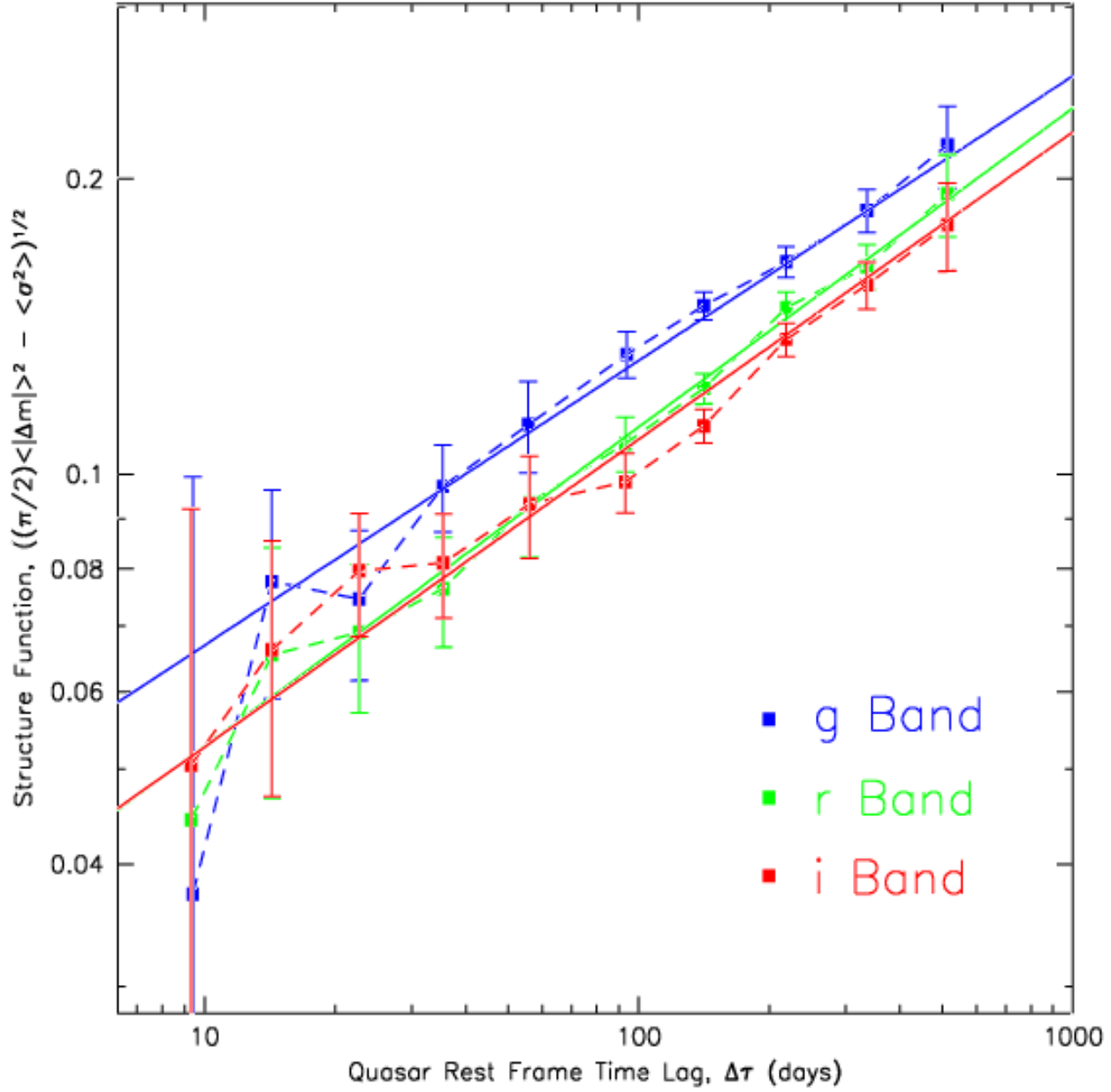


Fig. 8.— Quasar structure functions for each of the three pass bands, color coded by band. No accounting has been made for any other variability dependencies, such as luminosity, wavelength, or redshift. Single power law fits to the data are also shown.

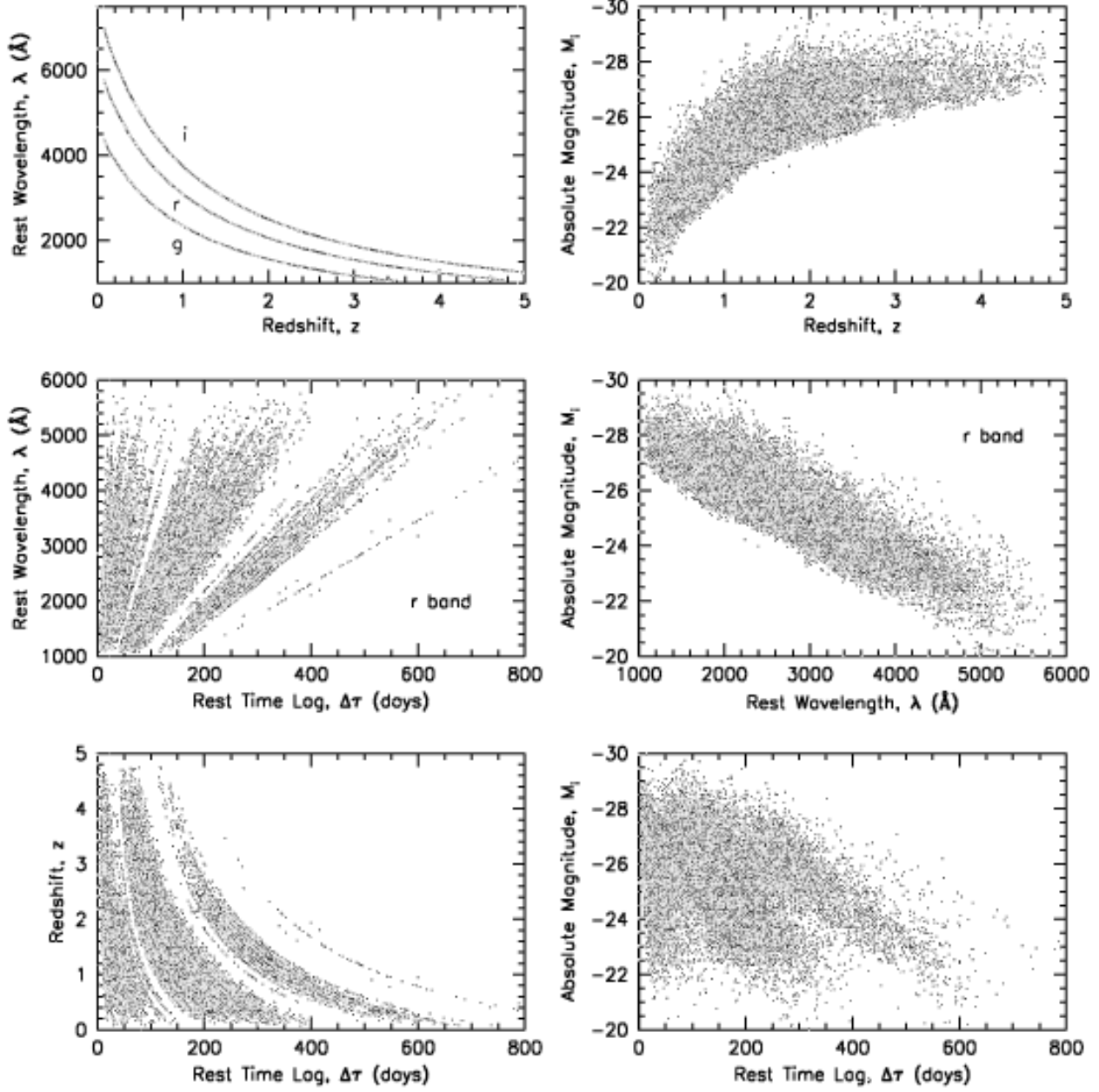


Fig. 9.— Projected parameter values for all of the quasars. This effectively shows the selection function in the parameter space given by rest frame time lag, $\Delta\tau$, redshift, z , absolute i -band magnitude, M_i , and rest wavelength, λ_{rest} . The passbands are indicated when necessary. For clarity, only the r band data are shown for the middle two plots.

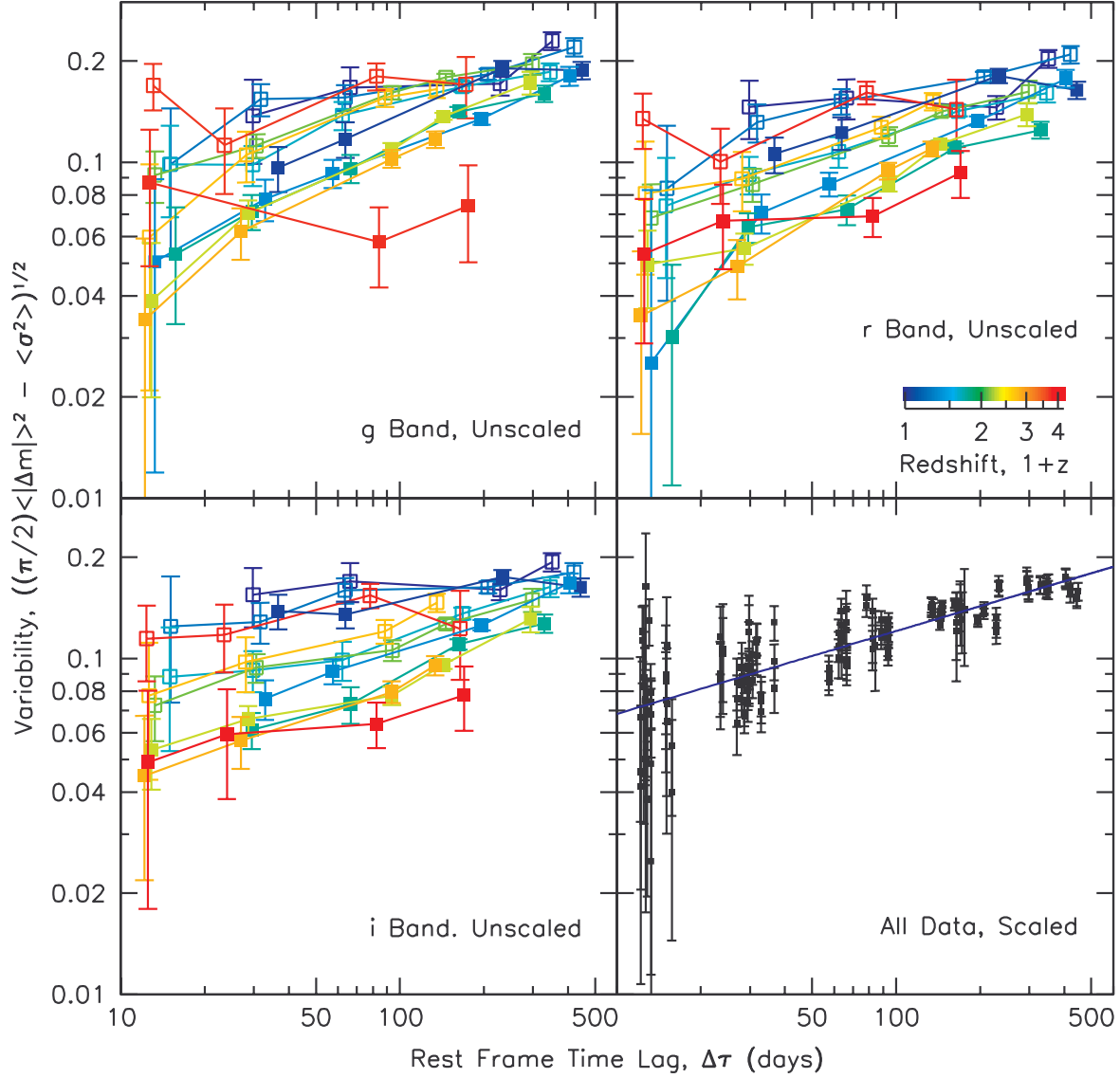


Fig. 10.— Variability as a function of rest frame time lag for independent slices of data (upper left, upper right, and lower left panels). Colors indicate redshift, with redder colors showing data from higher redshift ranges, according to the color key. Solid and open points show results from slices with higher and lower luminosities respectively, within the same redshift range. Results from the three photometric bands are given separately, which effectively restricts the rest wavelength ranges to small values in each slice. The lower right panel shows all of the scaled data points, along with the best fit power law for variability vs. $\Delta\tau$.

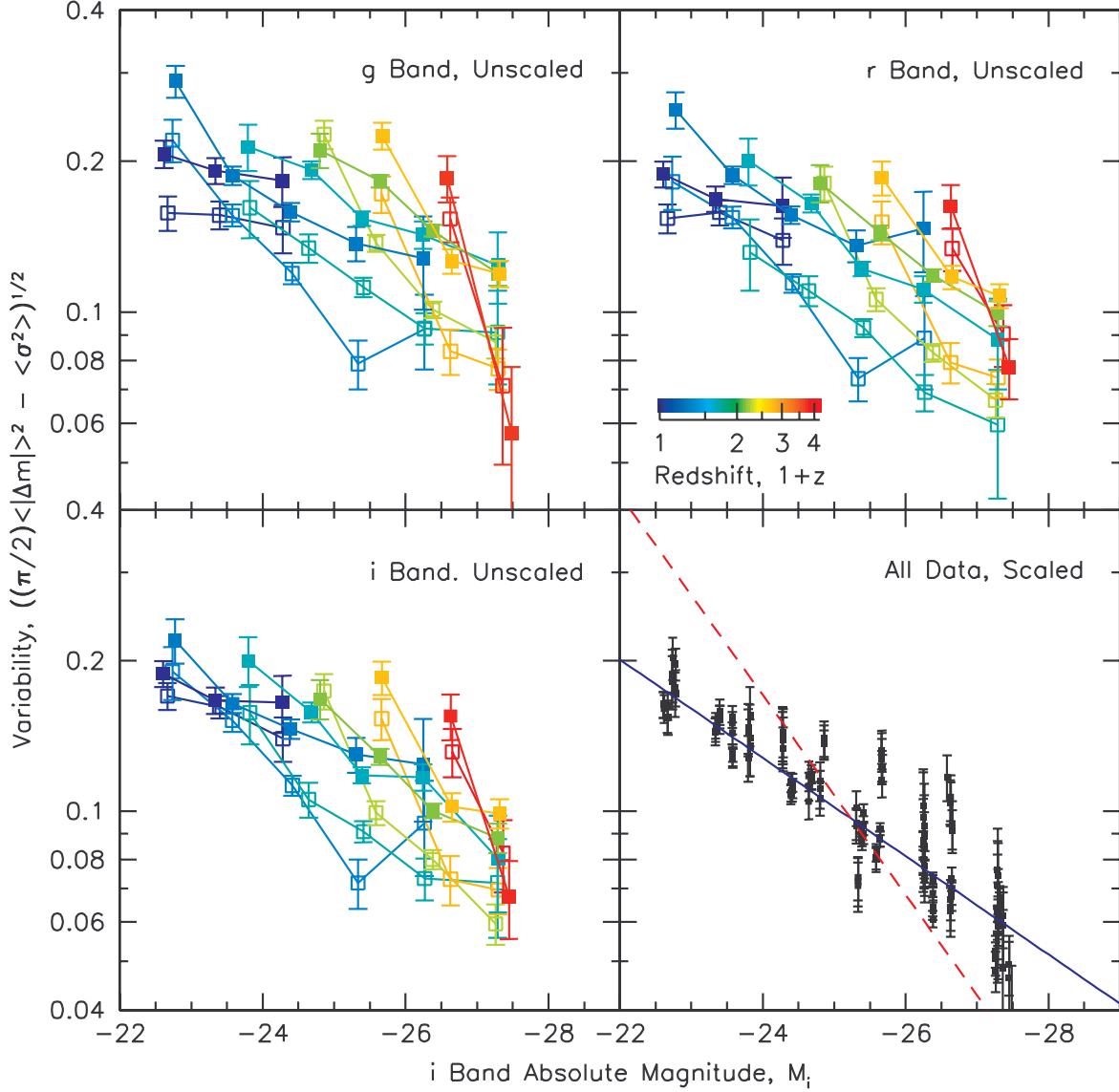


Fig. 11.— Variability as a function of absolute magnitude for independent slices of data (upper left, upper right, and lower left panels). Colors indicate redshift, with redder colors showing data from higher redshift ranges, according to the color key. Solid and open points show results from slices with longer and shorter time lags respectively, within the same redshift range. Results from the three photometric bands are given separately, which effectively restricts the rest wavelength ranges to small values in each slice. The lower right panel shows all of the scaled data points, along with a best fit generalized Poissonian function (solid) and Poissonian function with the power law index fixed at 1/2 (dashed).

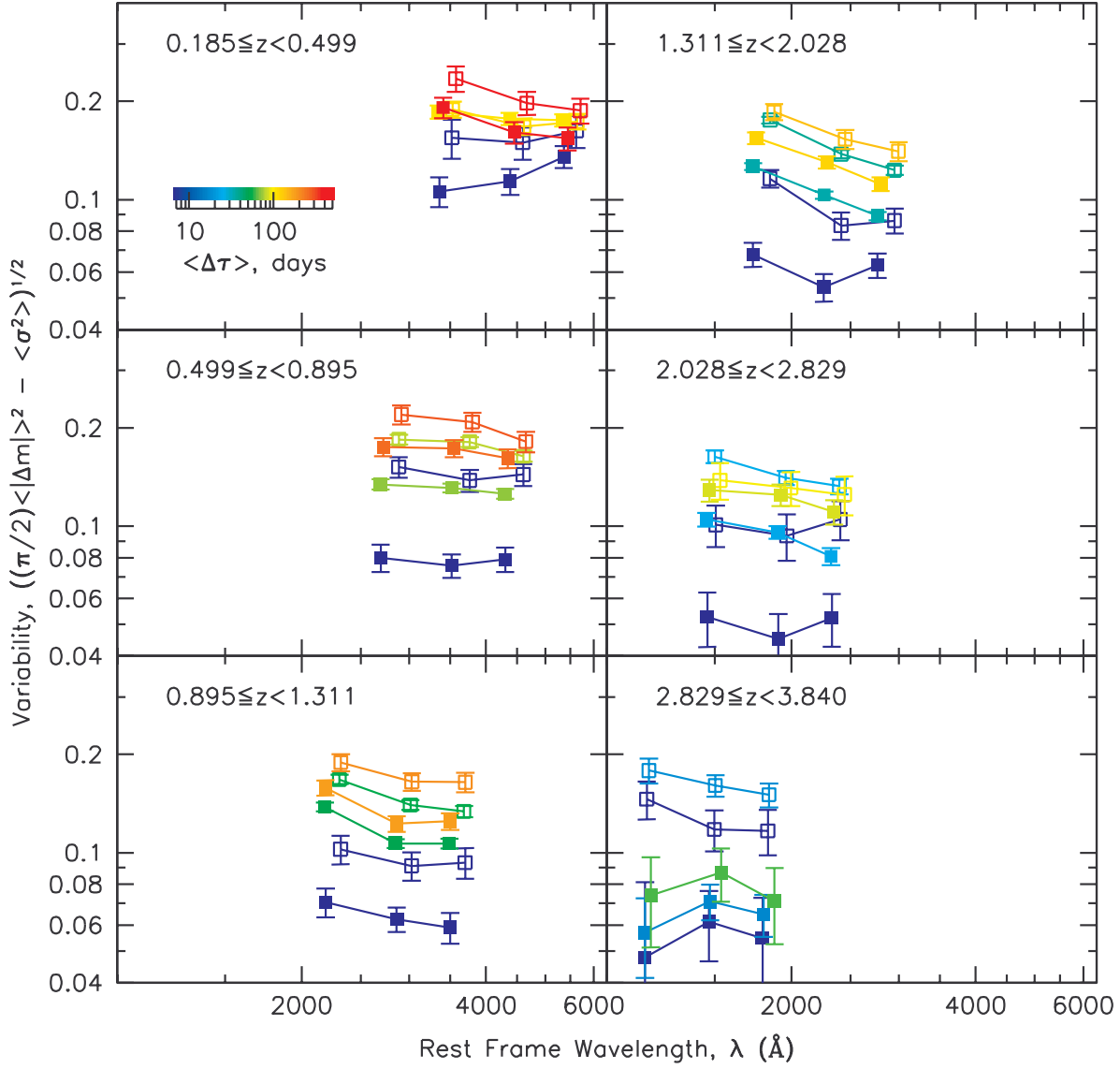


Fig. 12.— Variability as a function of rest frame wavelength for independent slices of data. Colors indicate average rest frame time lag, with redder colors showing longer time lags, according to the color key. Solid and open points show results from slices with more luminous and less luminous quasars respectively, within the same redshift and time lag ranges. Results from the six redshift slices are shown in separate panels.

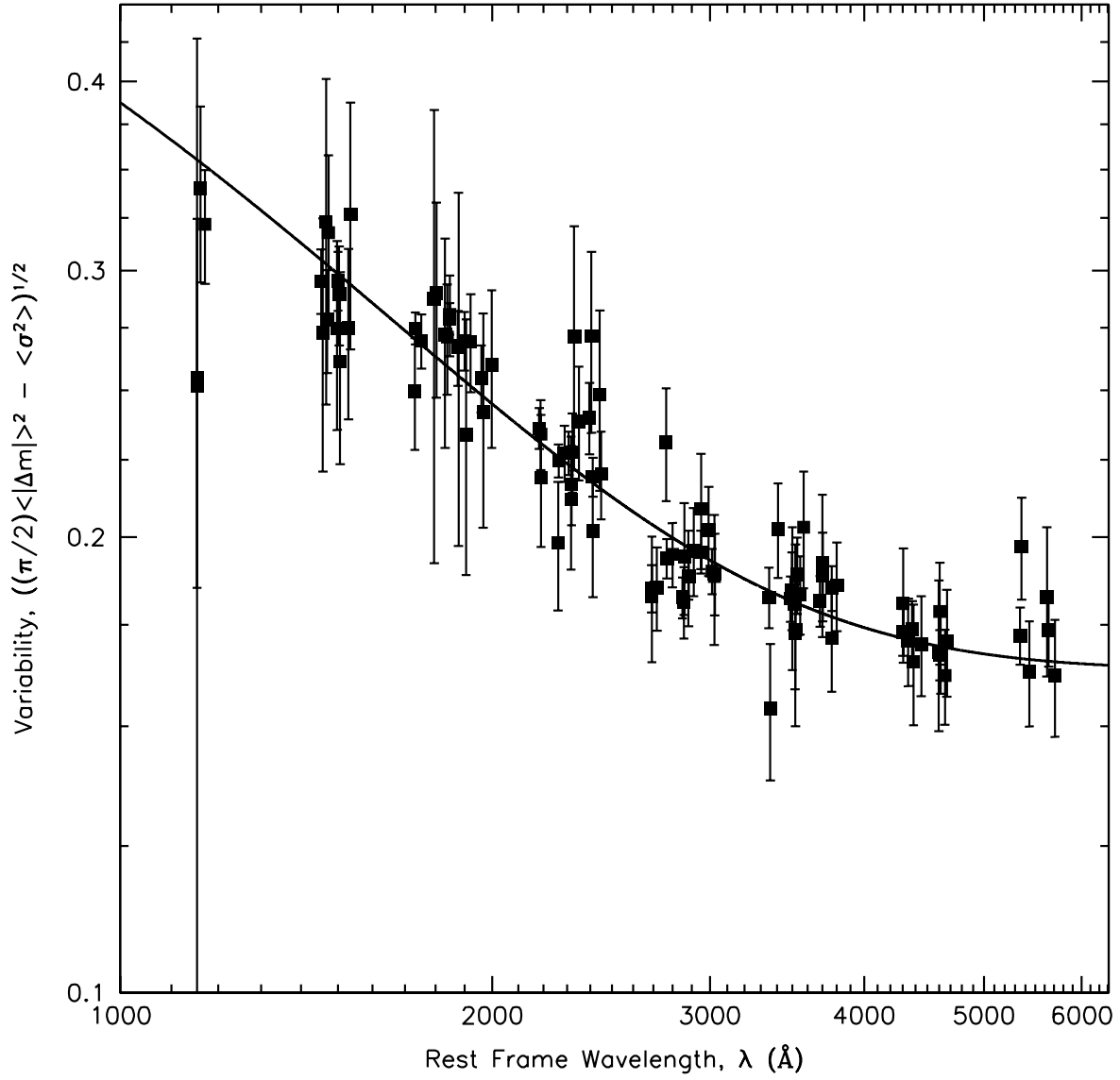


Fig. 13.— Scaled variability amplitude points from Fig. 12 as a function of rest frame wavelength. The line shows the best fit exponential function as described in the text.

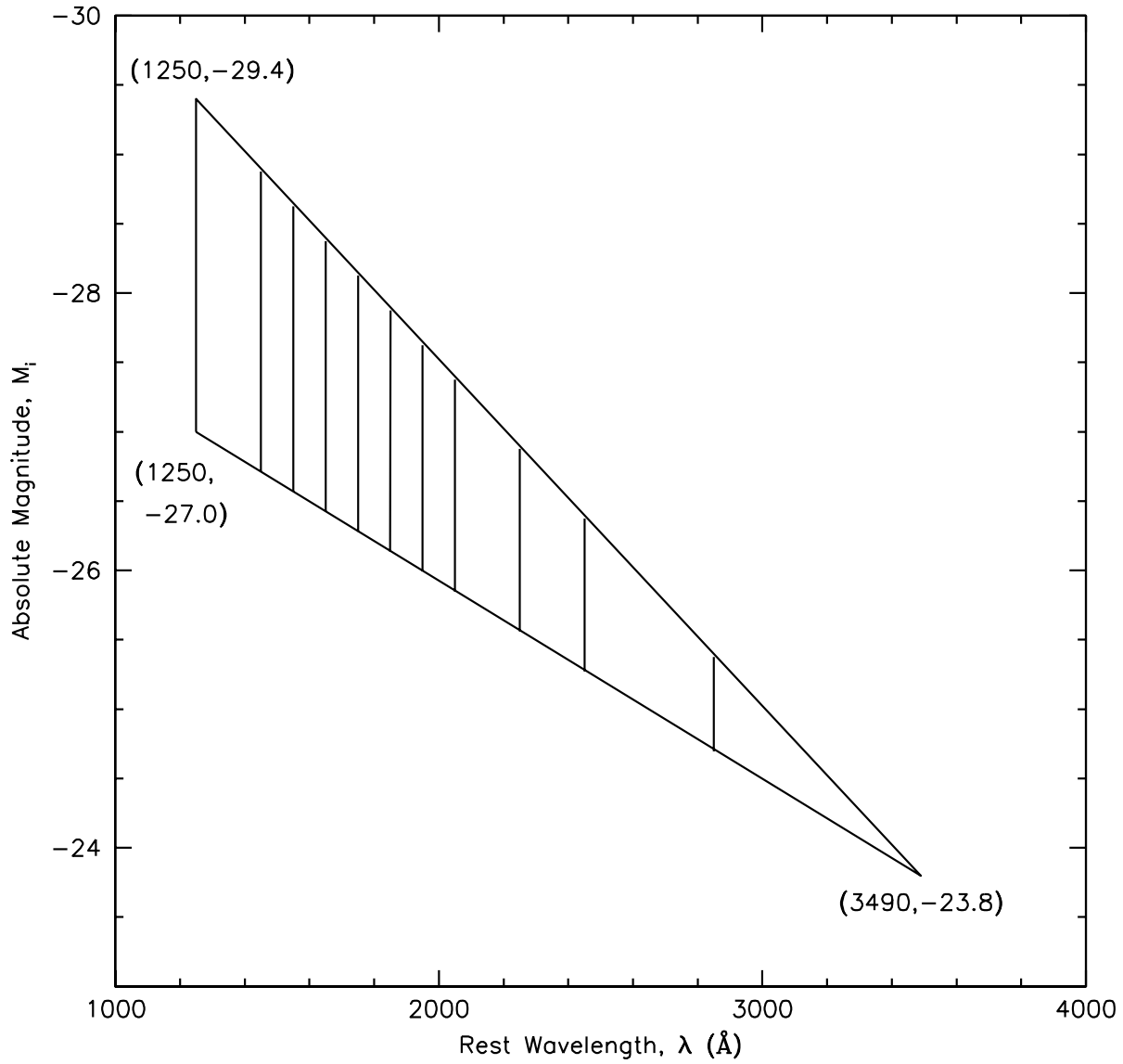


Fig. 14.— The triangle shows the region of the wavelength-absolute magnitude plane that is simultaneously well covered by quasar observations in all three photometric bands. The vertical lines – separated by 100, 200, 400, or 800Å – show the bin sides used to separate the quasar sample by wavelength.

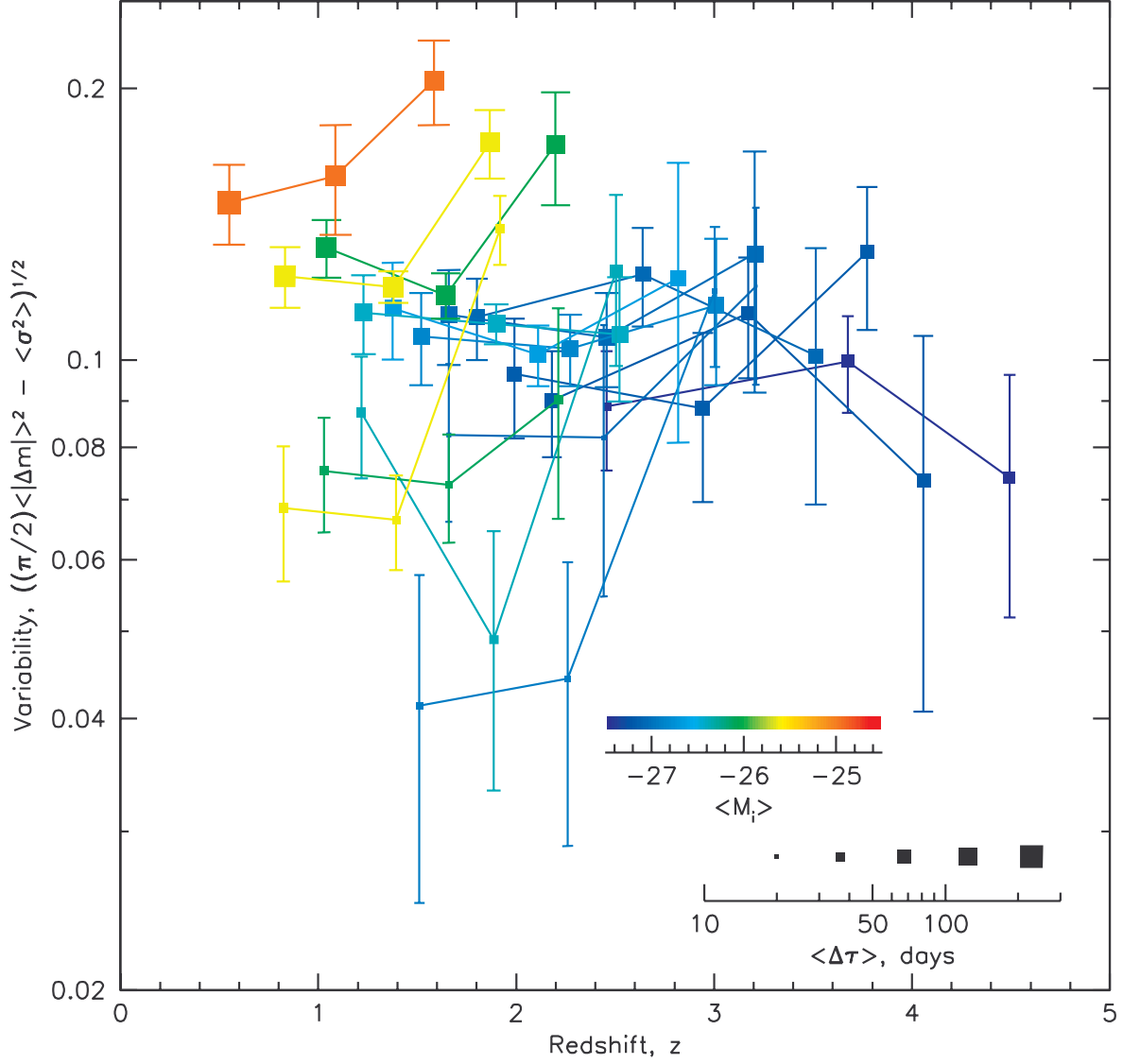


Fig. 15.— Variability as a function of redshift for independent sets of data. Sets of three connected points show the variability amplitude for data sets with similar distributions of rest wavelength, absolute magnitude, and time lag, but different average redshifts. Colors correspond to the average absolute magnitude for each set, with bluer colors indicating brighter absolute magnitudes, according to the color key. The point sizes correspond to average time lags, according to the point size scale.

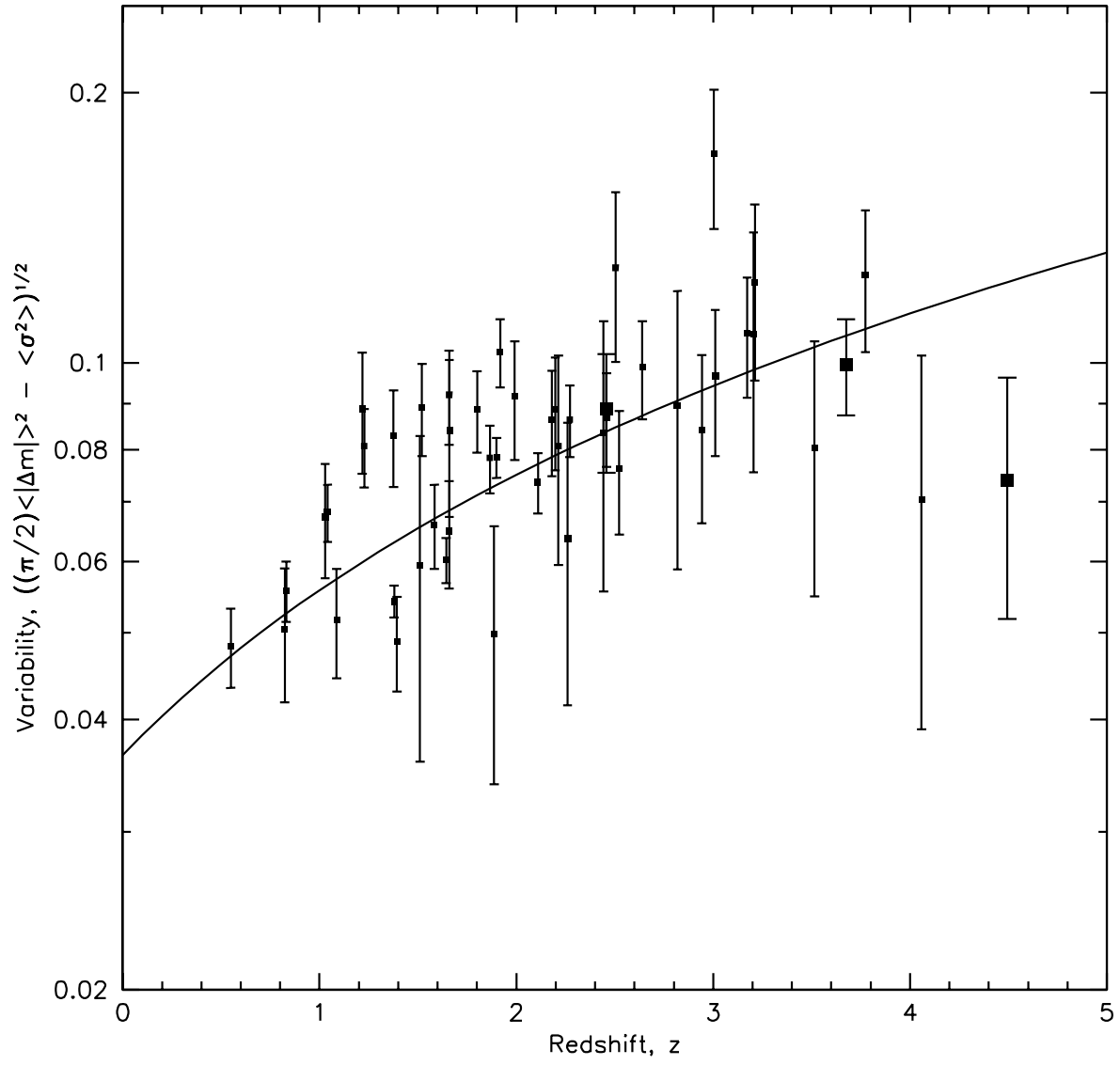


Fig. 16.— Scaled variability amplitude as a function of redshift. The best fit line (to linear redshift and variability amplitude) is also shown.

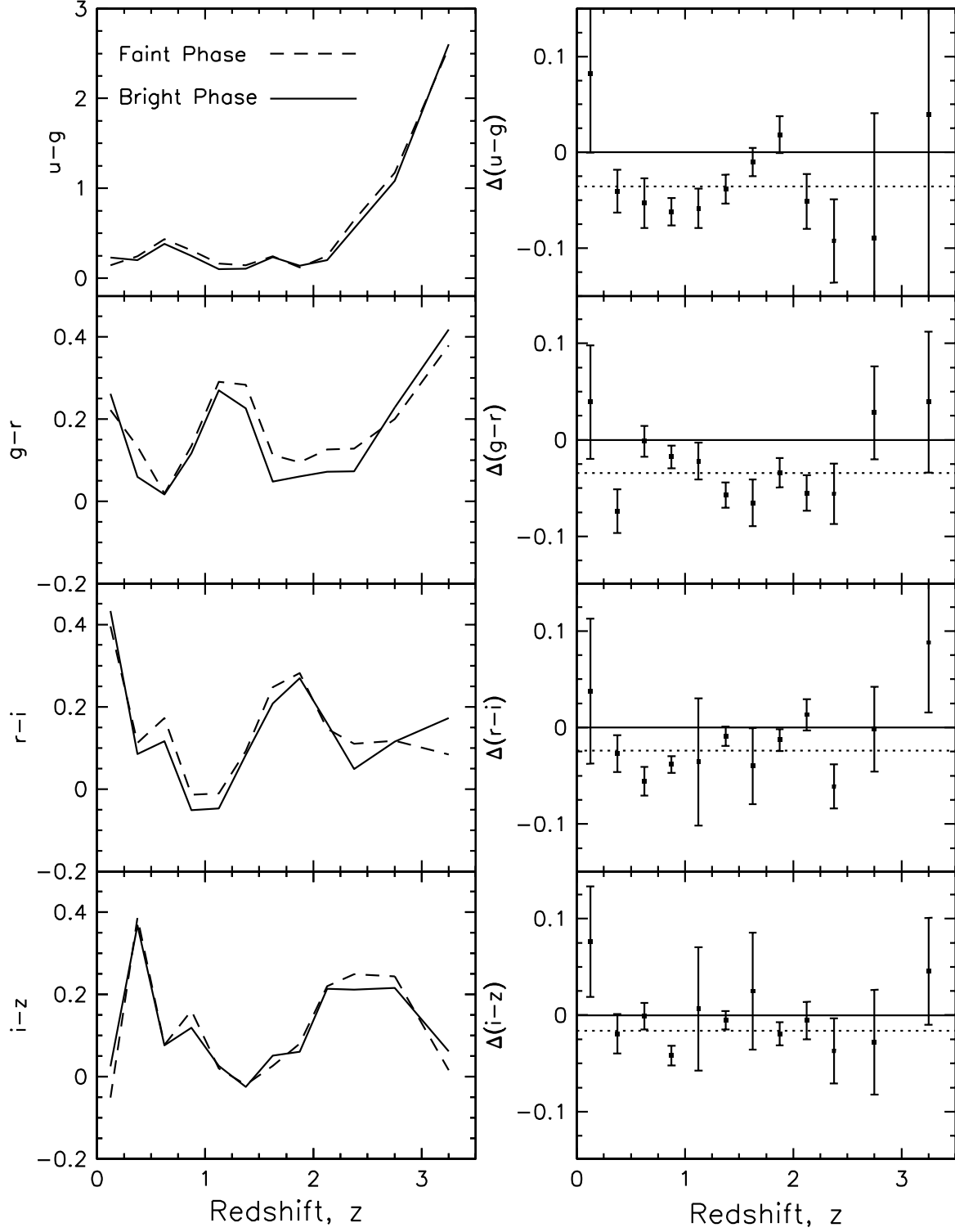


Fig. 17.— Average faint phase vs. bright phase colors of quasars as a function of redshift (left). The structure in the plots is mainly due to spectral features redshifting into and out of the various passbands. The plots on the right side show the color difference between the bright and faint phases as a function of redshift, along with the uncertainties in each bin. A more negative value implies a bluer spectrum in the

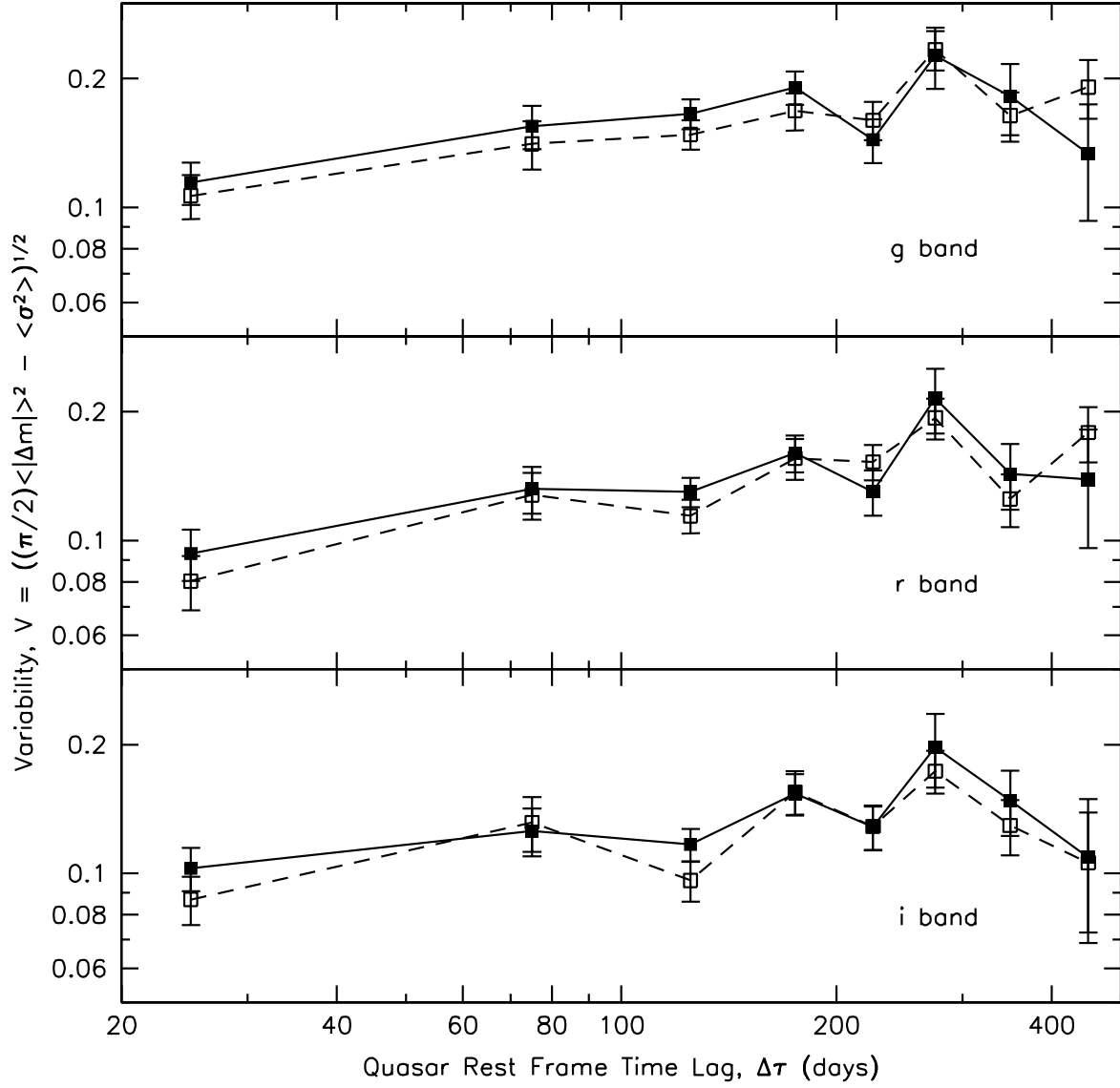


Fig. 18.— Radio-detected (solid lines and points) vs. undetected (dashed lines and open points) structure functions.

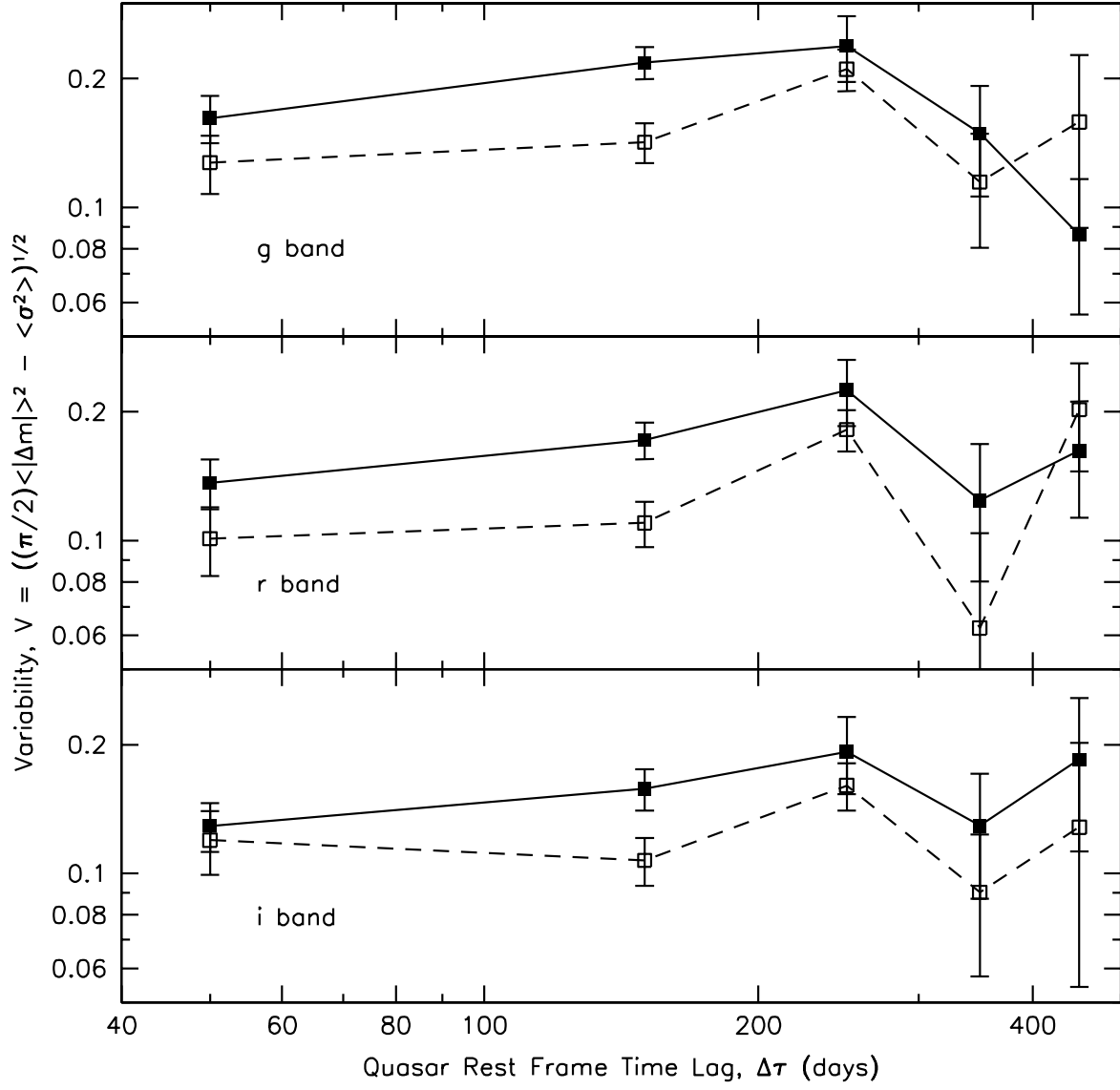


Fig. 19.— Radio-loud (solid lines and points) vs. radio-quiet (dashed lines and open points) structure functions.

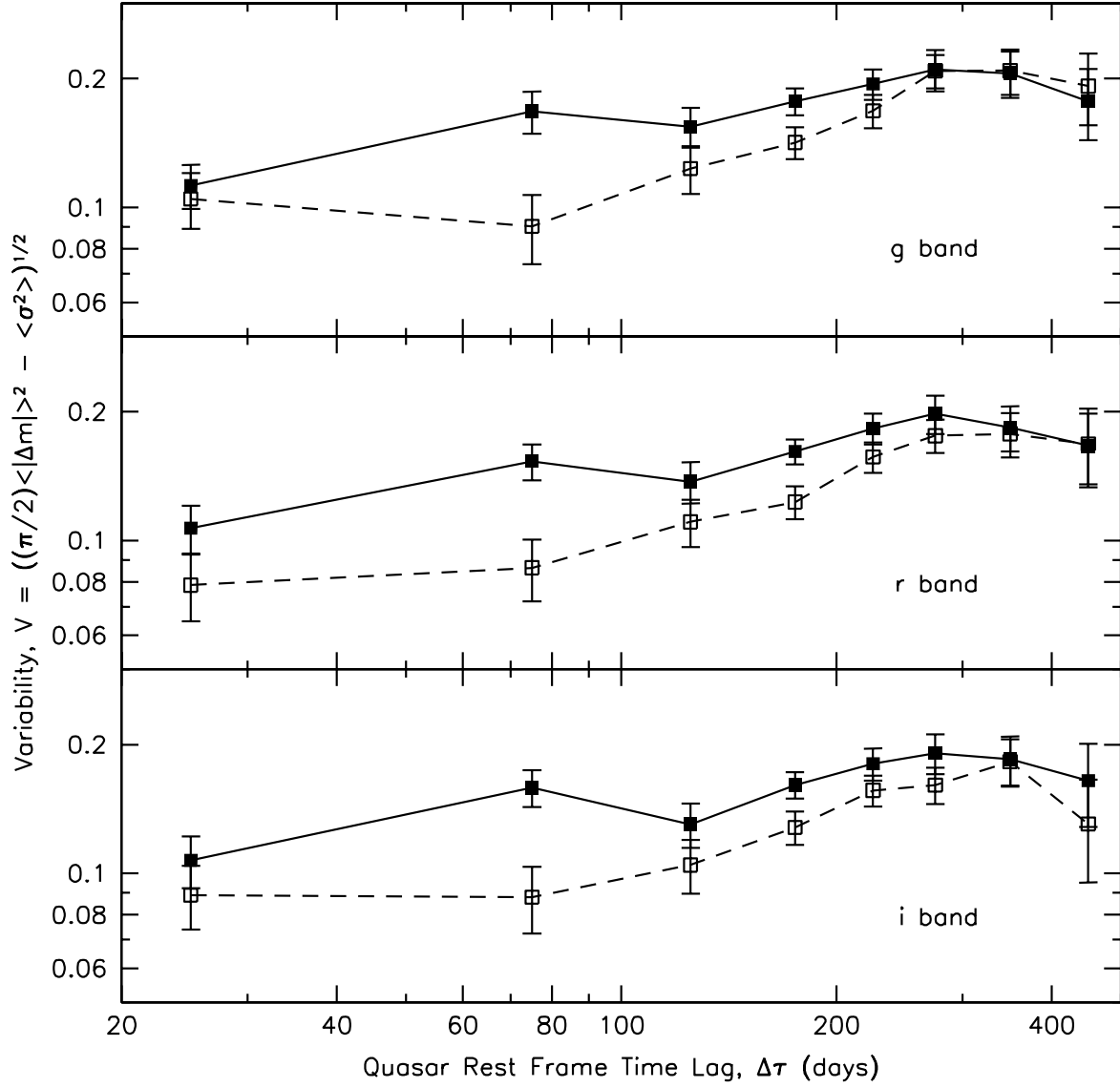


Fig. 20.— X-ray-detected (solid lines and points) vs. undetected (dashed lines and open points) structure functions.

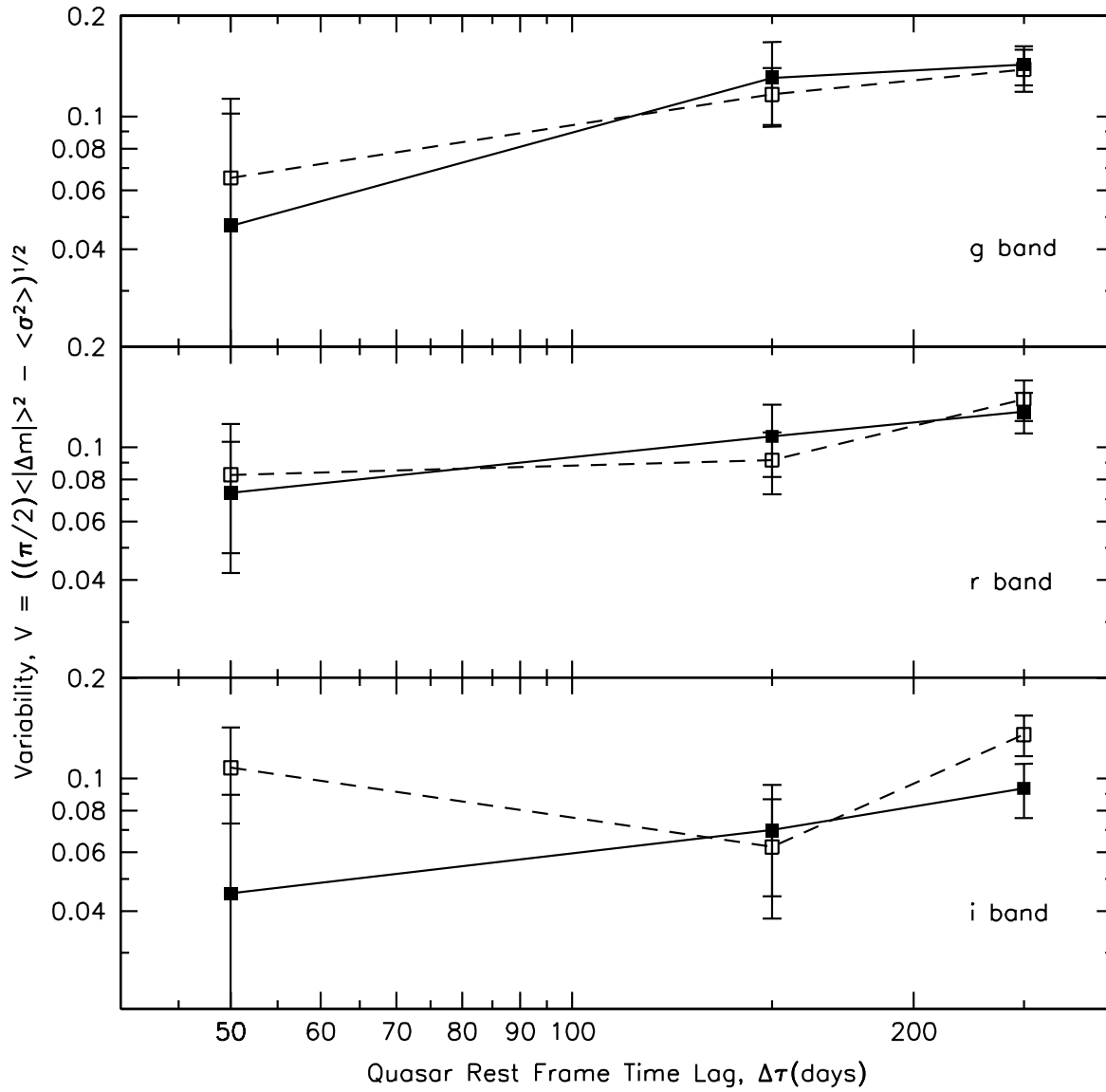


Fig. 21.— BALQSO (solid lines and points) vs. non-BALQSO (dashed lines and open points) structure functions.

TABLE 1
PARAMETER VALUES FOR FITS TO THE BINNED STRUCTURE FUNCTIONS.

Power Law			
Band	$\Delta\tau_0$ (days)	γ	χ^2
<i>g</i>	$9.90 \pm 6.49 \times 10^4$	0.293 ± 0.030	1.51
<i>r</i>	$7.05 \pm 4.23 \times 10^4$	0.336 ± 0.033	1.20
<i>i</i>	$1.66 \pm 1.32 \times 10^5$	0.303 ± 0.035	4.20
Exponential			
Band	V_0 (mag)	$\Delta\tau_0$ (days)	χ^2
<i>g</i>	0.168 ± 0.005	51.9 ± 6.0	20.5
<i>r</i>	0.155 ± 0.006	74.7 ± 8.9	24.8
<i>i</i>	0.139 ± 0.005	62.6 ± 8.3	39.3

TABLE 2
PARAMETER VALUES FOR FITS TO THE SCALED VARIABILITY TIME LAG DEPENDENCE.

Power Law		
$\Delta\tau_0$ (days)	γ	χ^2
$5.36 \pm 1.46 \times 10^5$	0.246 ± 0.008	299.0
Exponential		
V_0	$\Delta\tau_0$ (days)	χ^2
0.144 ± 0.001	40.4 ± 1.4	443.4